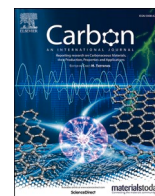# PŘÍLOHA I

Chem-mechanical polishing influenced morphology, spectral and electrochemical characteristics of boron doped diamond

M. Zelenský [a], J. Fischer [a], S. Baluchová [a], L. Klimša [b], J. Kopeček [b], M. Vondráček [b], L. Fekete [b], J. Eidenschink [c], F.-M. Matysik [c], S. Mandal [d], O.A. Williams [d], M. Hromadová [e], V. Mortet [b], K. Schwarzová-Pecková [a], A. Taylor [b,*]

[a] *Charles University, Faculty of Science, Department of Analytical Chemistry, UNESCO Laboratory of Environmental Electrochemistry, Albertov 2038/6, 128 00, Prague 2, Czech Republic*
[b] *FZU – Institute of Physics of the Czech Academy of Sciences, Na Slovance 1999/2, 182 21, Prague 8, Czech Republic*
[c] *University of Regensburg, Institute of Analytical Chemistry, Chemo- and Biosensors, Universitätsstraße 31, 93053, Regensburg, Germany*
[d] *Cardiff University, School of Physics and Astronomy, Queen's Buildings North Building, 5 the Parade, Newport Road, CF24 3AA, Cardiff, United Kingdom*
[e] *J. Heyrovský Institute of Physical Chemistry of the CAS, Dolejškova 2155/3, 182 23, Prague 8, Czech Republic*

A B S T R A C T

In this study complex characterization and comparison of as-grown and chemical-mechanical (CM) polished ultra-thin ($\leq$500 nm) boron doped diamond (BDD) electrodes with various boron content (0.58–4.4×10^{21} cm^{-3}, deposited with B/C 500–8000 ppm) was performed. Atomic force and scanning electron microscopy were used to compare morphological changes and confirm the reduction in roughness down to $\leq$2 nm. High-quality CM polishing enabled electron backscatter diffraction leading to the evaluation of grain size distribution (mean 0.3 μm) and preferred grain texture, {011}. X-ray photoelectron spectroscopy confirmed an increase in the B content on the surface of CM polished electrodes as a result of exposure of boron atoms incorporated into the bulk for highly doped BDD$_{4000}$ and BDD$_{8000}$ electrodes. Additionally, CM polished BDD electrodes are shown to possess uniform distribution of conductivity as proved by scanning electrochemical microscopy. This was reflected in faster heterogenous electron transfer kinetics for inner-sphere redox markers ([Fe(CN)$_6$]$^{3-/4-}$ and dopamine) and higher values of double layer capacitance in comparison with as-grown electrodes. These changes were more pronounced for low doped electrodes. Finally, the improvement in electrochemical characteristics was demonstrated by superior electroanalytical performance of CM polished BDD electrodes for dopamine detection.

1. Introduction

Boron doped diamond (BDD) electrodes, with sp^3 hybridized carbon, are a very perspective electrode material thanks to properties of diamond such as chemical inertness and hardness. The low capacitance of BDD layers leads to low and stable background currents, and thanks to the high overpotential of hydrogen and oxygen evolution reactions, they provide a wide potential window, particularly at positive potentials in aqueous media. All these properties make BDD electrodes a very useful material for electroanalytical applications [1–4]. Nevertheless, the electrochemical properties of BDD electrodes are highly influenced by many factors, *e.g.*, boron doping level, sp^2 carbon impurities, crystal orientation, grain boundaries, and surface termination (H-, or O-terminated surface) created by pre-treatment of BDD surfaces. Each of these

factors play a significant role in influencing heterogenous electron transfer (HET) kinetics, in particular for inner-sphere redox processes [5–9].

Boron concentration influences the conductivity of BDD layers, where the theoretical value for semiconductive/metallic-like conductivity transition is 2×10^{20} boron atoms cm^{-3} [10–13]. The boron dopant level is also related to the sp^2 carbon content in BDD layers, as with higher B/C ratio in the gas phase during chemical vapour deposition (CVD), crystalline quality diminishes and BDD layers possess higher grain boundary content. An increased sp^2 carbon/boron content increases the number of charger carriers in BDD layers, which results in an increase in background current and therefore shortens the potential window [11,14–16]. Further, it leads to acceleration of HET kinetics for inner-sphere redox systems [6,17–19]. However, unwanted adsorption

of reaction (by)products can occur due to higher sp^2 carbon content in highly doped BDD layers, which can cause surface fouling [20].

Surface termination is another crucial factor determining electrochemical properties of BDD layers. It can be easily varied by in-situ electrochemical pre-treatment of the surface. Cathodic pre-treatment in the potential region of hydrogen evolution leads to hydrophobic H-terminated surfaces possessing limited surface conductivity, while anodic pre-treatment in the region of water decomposition to hydroxyl radicals leads to O-termination [21,22]. These surfaces, containing –C–OH, –C=O, –C–O–C– and –COOH groups, are partially negatively charged, thus hydrophilic and their surface conductivity is minimal [2, 23]. Further, they exhibit slow HET kinetics for inner-sphere redox markers due to the presence of π-electrons in oxygen functional groups [24]. Another way to treat BDD surfaces is alumina polishing, which is commonly used on other solid electrodes. This procedure presumably leads to removal of sp^2 hybridized carbon possessing oxygen functionalities, thus alumina-polished layers have a lower content of oxygen functionalities as confirmed by X-ray photoelectron spectroscopy (XPS) [12]. This polishing process was, for a long time, considered as a process that could damage a surface and create defects which can trap charge carriers, however an increasing number of analytical studies on polished surfaces confirm its stability, sufficient signal reproducibility and sensitivity thanks to fast HET kinetics [6,25–27].

While alumina-polishing only affects the sp^2 hybridized carbon and the attached oxygen functionalities, it does not change the surface morphology. Chemical-mechanical (CM) polishing, which is capable of smoothing diamond crystallites, has been used for polishing of ultra-thin (≤ 500 nm) polycrystalline [28] and single crystal [29] undoped diamond. Here, an alkaline colloidal silica is used as a polishing fluid on a polyurethane/polyester pad. Quantum chemical simulations, on {110} surfaces, proved that strong C–O and C–Si bonds can be formed between silica and carbon atoms, which chemically activates C–C bonds between terminating carbon zigzag chains and bulk diamond. As a consequence, C–C bonds are broken, and carbon atoms can be extracted from the diamond lattice [30], leading to a final RMS surface roughness of <2 nm over large areas.

While CM polishing has been used on ultra-thin BDD layers in the past [31,32] for testing superconducting properties of BDD, or for thin (*ca* 2 μm) layers of highly doped BDD [9], the surface properties of BDD layers differing in boron content before and after polishing has not been investigated in detail. In this work a complex morphologic, spectral, and electrochemical characterization was performed to assess the effect of CM polishing in comparison with polycrystalline as-grown BDD electrodes deposited at B/C ratios of 500, 1000, 2000, 4000, 8000 ppm in the gas phase during CVD. A wide range of techniques including Raman spectroscopy, scanning electron (SEM) and atomic force microscopy (AFM), XPS, scanning electrochemical microscopy (SECM), electron backscatter diffraction (EBSD), electrochemical impedance spectroscopy (EIS), square wave voltammetry (SWV), and cyclic voltammetry (CV) for evaluation of HET kinetics of outer- and inner-sphere redox markers was used to assess the performance of CM polished BDD electrodes and to contribute to understanding of the interplay between the boron and sp^2 carbon content, oxygen content and morphology and physical and electrochemical properties of BDD.

2. Experimental

2.1. Synthesis of polycrystalline BDD layers

Polycrystalline BDD layers were deposited on 2-inch conductive Si wafers using a 1.5 kW resonance cavity microwave plasma enhanced CVD (MW PECVD) system (AX5010 from Seki Diamond Systems) using well established growth conditions, *i.e.*, 0.5% CH_4 in H_2, gas pressure = 50 mbar, microwave power = 1150 W, substrate temperature ca 750 °C and a growth duration of 5 h to produce layers with thicknesses ≤ 500 nm. Boron doping was obtained by the addition of trimethylboron in the

gas phase to give a B/C ratio ranging from 500 to 8000 ppm (BDD_{500} – BDD_{8000}). Prior to CVD, conductive Si wafer substrates were cleaned using acetone, isopropyl alcohol, H_2SO_4/H_2O_2 and rinsed in deionized water. Substrates were then seeded with a nanodiamond dispersion (NanoAmando®B) in water (0.2 g L^{-1}) using a spin coater. At each B/C ratio two Si wafers were BDD coated, one was left "as-grown" and the second was CM polished. CM polishing was carried out using a Logitech Tribo polishing system in conjunction with a SUBA-X polishing pad and Logitech supplied Syton SF-1 alkaline colloidal silica polishing slurry containing 15–50% SiO_2, 9.2–10.1 pH, 4–5% ethylene glycol [28]. Samples were polished until the RMS roughness was reduced to <2 nm. Samples grown with B/C ratios from 500 to 4000 ppm took 5–7 h, whereas the 8000 ppm sample took 2.5 h. An essential cleaning step followed CM polishing: BDD samples were dipped in HF (54%) to remove any residual colloidal silica polishing slurry. Thus, in this study as-grown BDD electrodes and CM polished BDD electrodes after HF treatment are compared, representing the as-obtained surfaces.

2.2. Chemicals

Hexaammineruthenium(II) chloride, dopamine hydrochloride, ferrocene(I) methanol (FcMeOH), potassium hexachloroiridate(III) (all Sigma-Aldrich, Germany), potassium hexacyanoferrate(II) trihydrate, potassium hexacyanoferrate(III), potassium chloride, sodium dihydrogen phosphate dihydrate (all Lach-Ner, Neratovice, Czech Republic), and sodium hydroxide (Penta, Chrudim, Czech Republic) were of analytical grade and used without any further purification. Deionized water (Millipore Mili plus Q system, Billerica, USA) with resistivity of not less than 18.2 MΩ cm was used to prepare all aqueous solutions. 0.10 mol L^{-1} phosphate buffer of pH 7.4 was prepared by adjusting with 0.50 mol L^{-1} NaOH to desired pH value.

2.3. Characterisation techniques

Morphological characterization was investigated by AFM and SEM. AFM measurements were carried out at room temperature using a Bruker, Dimension Icon system in Peak Force Tapping mode with ScanAsyst Air tips (Bruker; $k = 0.4$ N m^{-1}; nominal tip radius 2 nm). Measured topographies have 512×512 points resolution. To obtain roughness data areas of 1×1 μm^2 and 5×5 μm^2 were analysed. SEM was carried out using a TESCAN FERA3 GM with Schottky field emission cathode. Several morphological examinations before and after polishing were performed at an acceleration voltage of 5 kV (secondary electron imaging), whereas microstructural crystallographic orientation mapping was performed at an acceleration voltage of 10 kV using an electron backscatter diffraction (EBSD) detector. Data was obtained using a EDAX DigiView V EBSD camera and EDAX APEX acquisition software, and subsequently processed with EDAX OIM Analysis 8 software containing a Neighbour Pattern Averaging & Reindexing (NPAR) tool.

Surface and bulk chemical analysis was carried out using Raman spectroscopy and XPS. Raman spectroscopy was carried out at room temperature using a Renishaw InVia Raman Microscope at 488 nm and with a laser power of 6 mW. For determination of boron concentration, [B], the fitting tool at http://ofm.fzu.cz/raman-tool, which analyses characteristic Raman peaks at ca 1200 cm^{-1} and 1330 cm^{-1} attributed, respectively, to the Fano-shaped maximum of phonon density of states and zone-centre phonon line of heavily boron doped diamond, was used over the range of 1100–1500 cm^{-1}. Values for sp^3/sp^2 were obtained from fitting of Raman spectra, over the 1000–1700 cm^{-1} range, to obtain curve/peak integrated area values using Renishaw WiRe 3.2 software. Values were then used according to Ref. [33] to give a layer quality factor fq indicating sp^3/sp^2. XPS was carried out on a NanoESCA microscope (Omicron) using monochromatized Al Kα radiation (hν = 1486.7 eV). Peak deconvolution was made by KolXPD software with Voigt peaks on Shirley background. Overall instrumental resolution was 0.5 eV. XPS spectra of CM polished BDD were measured after HF

treatment, while as-grown BDD measurements followed MW PECVD H plasma treatment to assure H-termination of the surface.

SECM measurements were carried out with a 920C system from CH Instruments (Austin/TX, USA). The instrument was positioned on a dampening plate in a custom-made Faraday cage. The laboratory-constructed electrochemical cell was made from polytetrafluoroethylene. A three-electrode setup was applied consisting of the SECM probe (as the working electrode), a Ag/AgCl/3 mol L^{-1} KCl reference electrode (CH Instruments, Austin/TX, USA), and a platinum wire as the counter electrode. Platinum disk electrodes with electrode diameters of 12.5 and 25 μm and an RG value (defined as the ratio of the total tip radius and the radius of the active microdisk electrode) of >10 were used as SECM probes. BDD samples were mounted on the bottom of the electrochemical cell and the cell was levelled prior to imaging experiments. Measurements were conducted in 5 mL of a mediator solution (1.5 mmol L^{-1} of the respective mediator) with 1 mol L^{-1} KNO$_3$ as a supporting electrolyte. Solutions were not deaerated prior measurements. FcMeOH, ferrocyanide, ferricyanide, and hexaammineruthenium (III) were used as redox mediators. Probe approach curves (PACs) were measured at a fixed probe potential corresponding to the respective mediator: +0.3 V FcMeOH, +0.5 V for ferricyanide, +0.1 V for ferrocyanide, and −0.2 V for hexaammineruthenium(III). The maximum approach speed was 2.5 μm s^{-1} and quiet time was 15 s. Imaging experiments were conducted with the same fixed probe potentials, probe scan rate was 200 μm s^{-1}, and quiet time was 15 s. Areas covered in the images had a size of 500 × 500 μm^2 with a step size of 5 μm and were recorded in constant-height mode, corresponding to feedback currents of either 150 or 200% relative to the steady-state current in the bulk solution. Determination of k_{app}^0 values from SECM data was conducted according to the method reported by Wei et al. [34]. Several PACs per sample were conducted. Fitting of PACs with theoretical curves yields a k_{app}^0 value per approached spot. The diffusion coefficient used for [Ru (NH$_3$)$_6$]$^{3+/2+}$ was 5.5 × 10^{-6} cm^2 s^{-1} [35]. PAC parameters were: probe potential −0.3 V, quiet time 15 s, maximum approach speed 0.5 μm s^{-1}.

For CV and SWV measurements a three-electrode setup was used consisting of an Ag/AgCl/3 mol L^{-1} KCl reference electrode and a platinum wire as an auxiliary electrode (both Elektrochemické detektory, Turnov, Czech Republic). The working electrode was constructed by Si wafers coated with the BDD layer placed in a Teflon electrode body with rubber sealing. The exposed geometrical area of the electrode was 2.01 mm^2.

CV measurements were performed using an Eco-Tribo polarograph with PolarPro 5.1 software (Eco-Trend Plus, Czech Republic). SWV experiments were carried out using a Palm-Sens potentiostat with PSTrace 5.8 software (PalmSens BV, Houten, The Netherlands) using optimized parameters (amplitude A, frequency f, potential step ΔE_s) for (i) as-grown BDD$_{500}$: $A = 60$ mV, $f = 20$ Hz, $\Delta E_s = 8$ mV, (ii) as-grown BDD$_{4000}$: $A = 50$ mV, $f = 10$ Hz, $\Delta E_s = 4$ mV, (iii) CM polished BDD$_{500}$: $A = 120$ mV, $f = 10$ Hz, $\Delta E_s = 8$ mV, and (iv) CM polished BDD$_{4000}$: $A = 220$ mV, $f = 20$ Hz, $\Delta E_s = 3$ mV. EIS measurements were carried out using Autolab PGSTAT101 potentiostat with Nova 2.1 software (Metrohm Autolab B.V., Utrecht, The Netherlands). Impedance spectra were recorded in 1 mol L^{-1} KCl at a potential 0 V, amplitude 10 mV and within the frequency range from 100 kHz to 0.1 Hz. Data were fitted by the equivalent circuit (depicted in Fig. S10a) containing constant phase element (CPE) and the parameters N and Y^0 were evaluated. To normalize the Y^0 values the real surface areas A_{real} calculated from AFM measurement were used. EIS data in 1 mol L^{-1} KCl in the presence of 1 mmol L^{-1} [Fe(CN)$_6$]$^{3-/4-}$ were measured at the potential $E = +0.25$ V and were evaluated using the equivalent circuit depicted in Fig. S11a). Obtained CPE values only in 1 mol L^{-1} KCl worked as the reference values during the fitting in the presence of the 1 mmol L^{-1} [Fe(CN)$_6$]$^{3-/4-}$ redox system.

The apparent heterogenous electron transfer rate constant k_{app}^0 was calculated by the Nicholson method [36], based on the difference in potential of the anodic and cathodic peaks ΔE_p of redox species

according to Equation (1),

$$k_{app}^0 = \psi \left[\frac{\pi D_0 n F v}{RT} \right]^{1/2} \tag{1}$$

where ψ is a dimensionless parameter obtained from the logarithmic dependence of ψ on ΔE_p evaluated from CVs [36], D_0 is the diffusion coefficient, n is the number of electrons, F is the Faraday constant (C mol^{-1}), v is the scan rate (V s^{-1}), R is the gas constant (J K^{-1} mol^{-1}), T is the temperature (K), and the value of π is 3.14. Further, k_{app}^0 values were calculated from Tafel plots using Equation (2),

$$i^0 = nFA_{real}k_{app}^0 c \tag{2}$$

where i^0 is the exchange current obtained from Tafel plots (A), n is the number of electrons, F is Faraday constant (C mol^{-1}), A_{real} is the real exposed BDD area (cm^2), k_{app}^0 is kinetic constant (cm s^{-1}), c is concentration (mol cm^{-3}).

The following diffusion coefficients were used for particular redox markers: 7.6 × 10^{-6} cm^2 s^{-1} for [Fe(CN)$_6$]$^{3-/4-}$ [37], 5.5 × 10^{-6} cm^2 s^{-1} for [Ru(NH$_3$)$_6$]$^{3+/2+}$ [35] and 8.3 × 10^{-6} cm^2 s^{-1} for [IrCl$_6$]$^{2-/3-}$ [38]. Concentration dependencies for dopamine were constructed from the average of five replicate measurements for each concentration on each BDD electrode. Limits of detection (*LOD*) for SWV determination of dopamine were calculated as threefold of the standard deviation s of the peak currents ($n = 7$) of the lowest measurable concentration divided by the slope of corresponding concentration dependence.

3. Results and discussion

3.1. Nano-structural characterisation of BDD electrodes

AFM and SEM were used to obtain the micrographs of each as-grown and CM polished BDD electrode. Fig. 1 displays micrographs for BDD$_{500}$, BDD$_{1000}$, BDD$_{2000}$, BDD$_{4000}$ and BDD$_{8000}$ electrodes. The images for as-grown electrodes typically show a well-defined crystalline structure with well-defined facets up to a B/C ratio of 4000 ppm. At 8000 ppm the crystalline quality and grain size is diminished with a high grain boundary content. It is a well-known phenomenon that the grain size decreases as the boron concentration is increased beyond saturation [39]. This figure clearly highlights the change in morphology following CM polishing of the BDD layers. After the polishing the layer exhibits not only a smooth surface, but also a well-defined grain boundary content. SEM micrographs clearly show that following CM polishing, BDD grains contain numerous growth twins. Cross-sectional SEM images (see Fig. S1) show that only the minimum of material was removed during the CM polishing step. AFM RMS roughness measurements confirm that the roughness following CM polishing is dramatically reduced, see Table 1. In all cases, except one, the roughness is at or below 2 nm. The RMS roughness value for BDD$_{1000}$ is affected by holes in the layer, leading to an increase in measured roughness. These holes are most likely related to remnants of the original surface roughness. When investigated over a smaller area (1 μm × 1 μm) the RMS roughness for BDD$_{1000}$ was found to be also <2 nm. The reduced RMS roughness of the as-grown BDD$_{8000}$ sample was reflected by the reduced CM polishing time, *i.e.*, less material was needed to be removed to reduce the RMS roughness to <2 nm.

Orientation mapping using EBSD was carried out on the CM polished BDD$_{2000}$ sample. The high-quality CM polishing and signal collection conditions enabled the acquisition of Kikuchi patterns on ultra-thin BDD layers, we believe, reported for the first time, however their acquisition remains complicated on diamond samples. Therefore, the conventional approach for this method was modified for such material. An example of a Kikuchi pattern can be seen in Fig. 2a) and an orientation map of the surface in Fig. 2b). After data processing using available tools (NPAR, pattern contrast improvement and indexation filtering) there is a visible
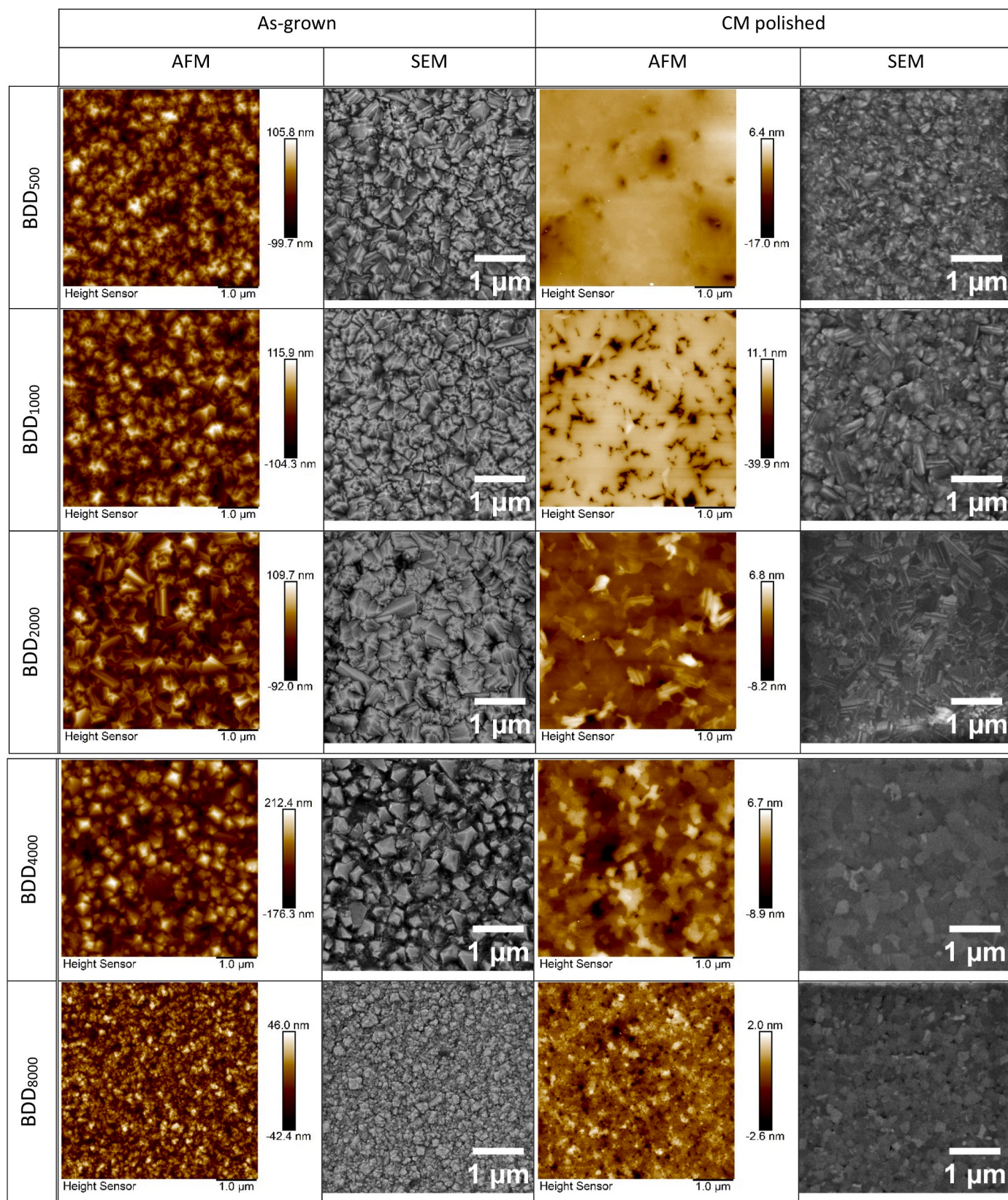
Fig. 1. AFM and SEM micrographs of as-grown and CM polished BDD_{500}, BDD_{1000}, BDD_{2000}, BDD_{4000} and BDD_{8000} electrodes. (A colour version of this figure can be viewed online.)

Table 1
RMS roughness and real surface area values from AFM (5 μm × 5 μm) measurements of as-grown (AG) and CM polished (CMP) BDD electrodes.

Sample	AFM – RMS roughness (nm)		Surface area difference (%)		A_{real} (cm^2)	
	AG	CMP	AG	CMP	AG	CMP
BDD$_{500}$	25	1.3	17.1	0.0291	0.0235	0.0201
BDD$_{1000}$	32	6.2	19.2	1.18	0.0240	0.0203
BDD$_{2000}$	32	1.5	18.1	0.0507	0.0237	0.0201
BDD$_{4000}$	54	2.2	37.7	0.199	0.0277	0.0201
BDD$_{8000}$	15	0.6	17.5	0.0561	0.0236	0.0201

equiaxed microstructure with a Gaussian grain size distribution, Fig. 2c). The grain size was measured to be 0.3 ± 0.1 μm. Grain orientations are not distributed randomly, but instead a strong texture is present with the strongest component having {011} along with a contribution from {111}, Fig. 2d).

3.2. Spectral characterisation of BDD electrodes

Raman spectroscopy is a useful tool for estimating the composition of BDD layers. It is capable of evaluating the boron doping level, which is incorporated in the layers, as well as the presence of non-diamond carbon. Fig. S2 shows typical Raman spectrum for low to high boron containing electrodes with boron related bands at *ca* 480 cm^{-1} and 1200 cm^{-1}, and a red shifted (from *ca* 1330 cm^{-1} down to *ca* 1282 cm^{-1}) Fano shaped diamond Raman line. The contribution from non-diamond phase bands at 1520 cm^{-1} can be seen to be rather constant with B/C ratios up to 2000 ppm, at 4000 and 8000 ppm this contribution increases. In addition, peaks related to the Si substrate are visible at 520 cm^{-1} and 950 cm^{-1}. The diamond red shift is increasing with higher boron doping levels and is associated with phonon confinement effect caused by the high concentration of boron defects and negative asymmetric coefficient with the Fano effect. The determined [B] concentration was established to be from 0.58×10^{21} cm^{-3} for BDD$_{500}$ electrodes up to 4.4×10^{21} cm^{-3} for BDD$_{8000}$ electrodes [40,41], for exact values of
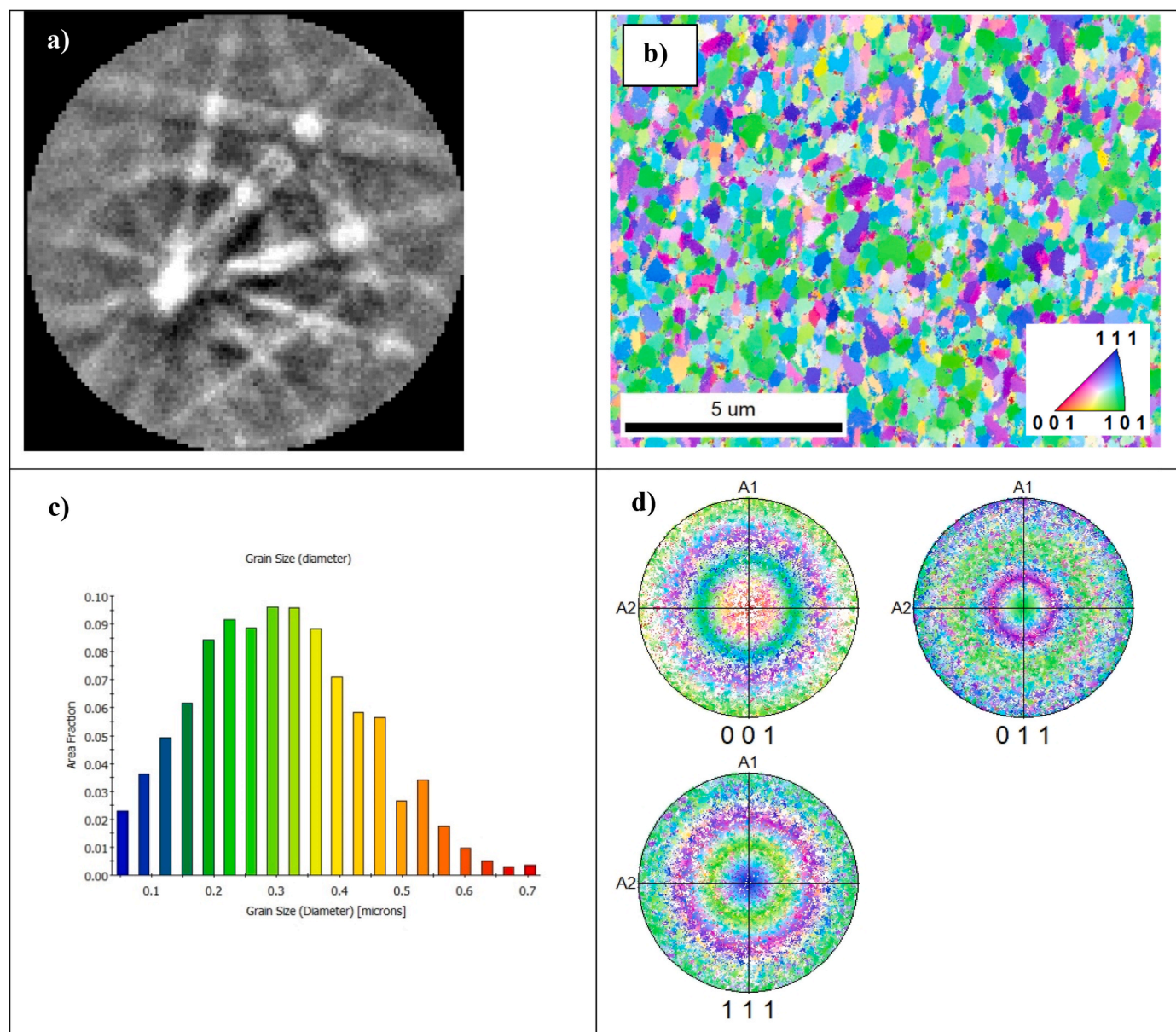

Fig. 2. Orientation image maps of CM polished BDD$_{2000}$ electrode: a) example of obtained Kikuchi pattern; b) grain orientation map; c) grain size distribution histogram; d) pole figures for {001}, {011} and {111} planes. (A colour version of this figure can be viewed online.)

as-grown and CM polished BDD see Table S1. All values are above the theoretical threshold of $[B] \approx 2 \times 10^{20}$ cm^{-3} for metallic-like conductivity [11]. After CM polishing the Raman spectra remained the same without any significant change (see Fig. S2).

XPS was carried out on all as-grown and CM polished BDD electrodes, obtained O 1s, C 1s and B 1s spectra are depicted in Fig. 3. They show the elementary content to be 98.9–95.7%, 0.23–4.79% and 0.7–1.9%, respectively in as-grown samples. After CM polishing, a rise in oxygen content, 4.4–6.3%, is observed, as summarized in Table 2. This can be expected following the strong oxidizing hydrofluoric acid cleaning step, applied to remove any residual silica slurry used for CM polishing, and may also support the proposed mechanism of polishing in Ref. [28], which suggests that due to wet oxidation of the surface during CM polishing, the amount of carbonyl and hydroxyl groups increases on the surface. In the samples with the highest B doping, the content of B rose by 0.3–1% of the total. Figs. S3a–c) show, as an example, detailed fitting of O 1s, C 1s and B 1s spectra for the BDD$_{2000}$ electrodes, as-grown and after CM polishing. Fitting of the O 1s spectra for both electrodes provide two components. Peak I. can be assigned to C–O and the peak II. is likely related to COOH functional groups [42]. C 1s spectra show several peaks. Peak I. corresponds probably to B$_4$C or B$_3$C. Peaks II. and III. are difficult to separate especially on CM polished electrodes, but these peaks can be attributed to sp^2 or sp^3 carbon C–C bonds and peak IV. to sp^3 C–H bonds [43]. Peak V. correlates with C–O. The final visible peak VI. occurring only on CM polished electrodes is related to COOH functional groups [12,44,45]. Following CM polishing C 1s spectra shows an overall increase in sp^2/sp^3 carbon content. This may be caused by introduction of C=O functional groups on the surface layer. B 1s spectra shows three peaks where peak I. may correspond to boron clusters, and peaks II. and III. correlate with B–C and B–H bonds respectively. The increase in [B] content of the highest doped electrodes after CM polishing could contribute to the explanation of the improved electrochemical performance and overall conductivity, as demonstrated below. An explanation for this could be a "shut-down" effect, where diamond deposition continues during the switch off procedure following CVD, *i.e.*, reduction in microwave power and gas flows, leading to a surface with lower [B], which after CM polishing reverts to the bulk [B]

Table 2

Values for C, B and O as measured by XPS of as-grown (AG) and CM polished (CMP) BDD electrodes.

Sample	C (%)		B–C contribution to C (%)		B (%)		O 1s (%)	
	AG	CMP	AG	CMP	AG	CMP	AG	CMP
BDD$_{500}$	97.9	95.4	0.23	0.22	0.25	0.19	1.9	4.4
BDD$_{1000}$	98.9	94.4	0.56	0.55	0.41	0.33	0.7	5.3
BDD$_{2000}$	97.7	93.7	1.14	1.01	0.67	0.66	1.6	5.7
BDD$_{4000}$	96.3	91.8	3.57	4.14	2.41	2.68	1.3	5.6
BDD$_{8000}$	95.7	90.0	4.79	5.25	2.71	3.69	1.6	6.3

content. Overall, it can be said that CM polished electrodes have a higher surface quality (lower inelastic background in spectra and higher and narrower peaks comparing to the as-grown electrode) in comparison with the as-grown electrodes.

The evaluation of data obtained from Raman and XPS measurements enables further estimation of [B] values and a rough evaluation of sp^2 carbon content. The values obtained using both methods are listed in Table S1. [B] bulk (Raman) and surface (XPS) values match quite well, with the same trend, *i.e.*, [B] increases with B/C as obvious from Fig. S4a). Bulk [B] values are consistent for as-grown and CM polished electrodes. The same can be said for surface [B] values at low B/C, whereas at higher B/C (4000 and 8000 ppm) there is a clear increase in [B] following CM polishing, due to the mentioned "shut-down" effect.

The qualitative value of bulk sp^3/sp^2 from Raman is indicated by layer quality factor *fq*. The contribution from non-diamond carbon at 1520 cm^{-1} can be seen to be rather constant in as-grown and CM polished electrodes with B/C ratios up to 2000 ppm (*fq* ≥ 96), at 4000 and 8000 ppm this contribution increases (*fq* ≤ 93), as seen in Fig. S4b). For XPS, to give a qualitative value for surface sp^3/sp^2 fitting was attempted on the C 1s spectrum. However, fitted peaks, II. (sp^2) + III. & IV. (sp^3), are not fully resolved leading to highly speculative values, from which no clear trend appears, see Fig. S4b). If peak I. at ~283 eV, is assumed to be sp^2 related, as in Ref. [46] or at least partly related, then a trend can be found, *i.e.*, that sp^2 content increases with B/C, see Fig. S4c) This agrees with Raman data, *i.e.*, decrease in sp^3/sp^2 with increasing B/C,
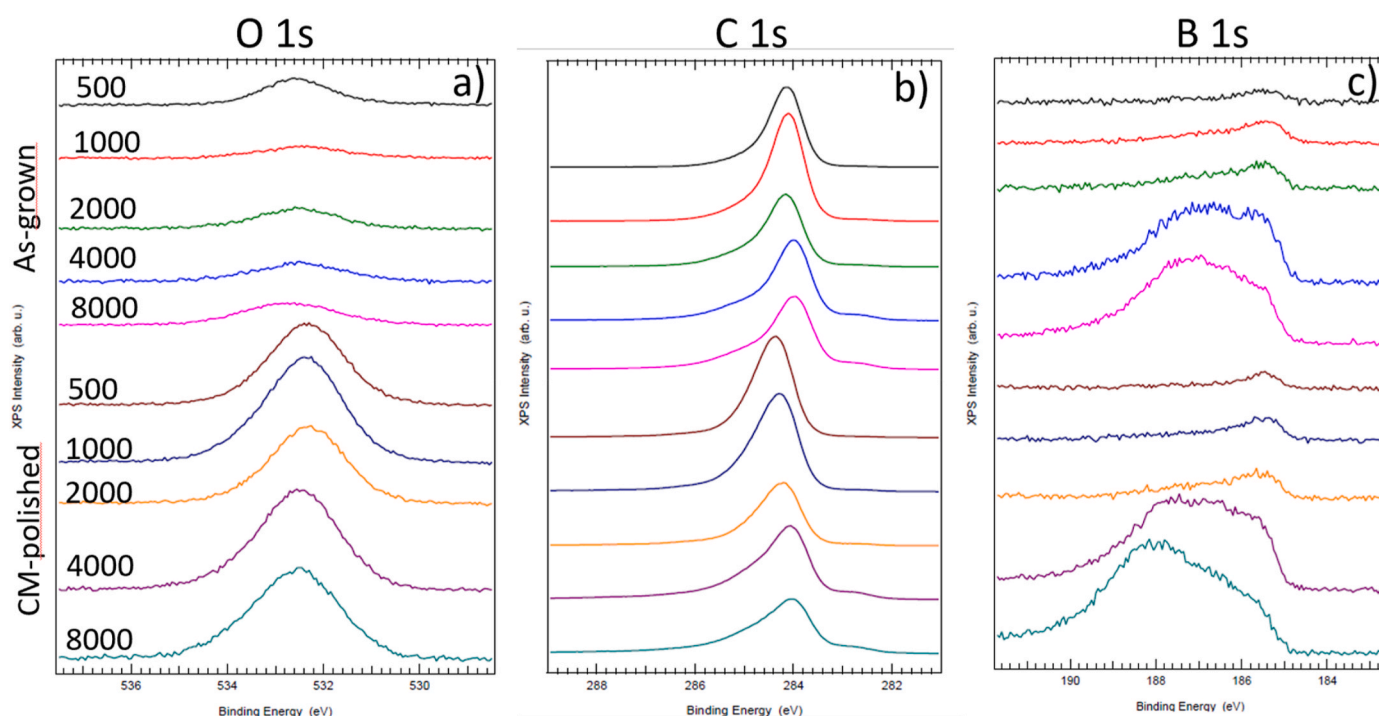

Fig. 3. a) O 1s, b) C 1s and c) B 1s XPS spectra of all investigated electrodes, in the order from top to bottom: As grown BDD$_{500\ to\ 8000}$ and CM polished BDD$_{500\ to\ 8000}$.

and SEM observations, *i.e.*, reduction in grain size and hence larger grain boundary content, especially when B/C = 8000 ppm. However, as further discussed in Section 3.4, no sp^2 related features are visible from an electrochemical point of view, therefore it is not clear how relevant or reliable these findings are.

3.3. Scanning electrochemical microscopy

Feedback mode in SECM was utilised to investigate the electrochemical surface activity of BDD electrodes on the microscale. These measurements were performed in 1 mol L^{-1} KNO$_3$ at substrate potentials where surface interaction of the NO$_3^-$ ions with C–H on the surface [47] of BDD presumably does not influence the electrochemical activity. The topographical influence on the SECM signal could be ruled out, as AFM measurements confirmed that the surface roughness was on the nm scale. Therefore, SECM measurements were performed in constant-height mode. At first, four commonly used redox mediators were evaluated for their suitability. Fig. S5 shows SECM images of the same area on the as-grown BDD$_{4000}$ sample recorded in different mediator solutions. By using outer-sphere redox mediators (FcMeOH and hexaammineruthenium(III)), surface details could be resolved well, while the use of inner-sphere redox mediators (ferri- and ferrocyanide) resulted in rather poor image quality. The same experiments were also conducted on the CM polished BDD$_{4000}$ electrode, here the image quality recorded with the outer-sphere mediators was comparable to the ones with the inner-sphere mediators. Further comparison of the two sets of BDD electrodes was carried out with FcMeOH, since it resulted in the overall highest image quality. In Fig. 4, typical PACs toward the as-grown BDD$_{8000}$ electrode and a SECM image are shown. During the approach toward the surface, positive as well as mixed feedback was observed. The red PAC in Fig. 4a) shows a PAC with positive feedback, typical for a conductive surface. In contrast, the blue PAC indicates an initial slight increase in the current when approaching the sample surface followed by a sharp current decrease near the BDD surface, resulting in negative feedback, typical for an insulating surface. This behaviour was found solely on as-grown electrodes and not on CM polished electrodes. In Fig. 4b) the corresponding destinations of the PACs are highlighted in red and blue.

In Fig. 5, SECM images of the surfaces of as-grown and CM polished BDD$_{500}$, BDD$_{2000}$, and BDD$_{8000}$ electrodes are shown in uniform normalized current scale. The surface activity of as-grown BDD was shown to be heterogeneously distributed, exhibiting spots of high electrochemical activity, mixed with spots of insulating properties. As expected, with increasing boron doping, the number of conductive spots increased. CM polishing was found to lead to a much more uniform distribution of surface activity, especially at high boron doping. It is known that boron atoms are uniformly distributed in depth of BDD layers regardless of boron concentration, as confirmed by secondary ion mass spectrometry and elastic recoil detection [43–45]. The exposure of uniformly distributed bulk boron atoms on the surface of CM polished electrodes is thus reflected in uniformity of their conductivity. However, still the CM polished samples were shown to have some variation in this electrochemical activity as is obvious from Fig. S6, which shows SECM images with a narrower current scale.

The range of k_{app}^0 values further characterizing electrochemical surface activity was calculated from seven individual PACs towards different positions on the BDD$_{4000}$ electrodes. For as-grown BDD, k_{app}^0 values ranging from 0.113 up to 0.313 cm s^{-1} were calculated, while for CM polished BDD$_{4000}$ electrode the values yielded a range from 0.280 to 0.382 cm s^{-1}. Overall, the CM polished sample seems to have a higher electrochemical activity, as well as a more homogeneous distribution shown by a narrower range of k_{app}^0 values. Homogeneity is also expressed by the lower variance of k_{app}^0 values for CM polished in comparison with as-grown BDD.

3.4. Electrochemical characterization of BDD electrodes

Electrochemical characterization of as-grown BDD and CM polished BDD electrodes (BDD$_{500}$ – BDD$_{8000}$) was performed to evaluate the effect of surface smoothing on HET kinetics and capacitance obtained from EIS measurements. CV measurements in 1 mol L^{-1} KCl in the presence of outer- ([IrCl$_6$]$^{2-/3-}$ and [Ru(NH$_3$)$_6$]$^{3+/2+}$) and inner-sphere ([Fe (CN)$_6$]$^{3-/4-}$, dopamine/dopamine-*o*-quinone) redox markers were performed for this purpose. The surface of the electrodes was kept in the as-grown and as-polished states (after HF treatment to remove residual silica used for CM polishing) by avoiding potentials leading to water electrolysis and thus surface oxidation/reduction. Re-hydrogenation of the CM polished surface was not attempted, as the stability of H-termination obtained using cathodic polarization or H-plasma treatment and their effectiveness for CM polished BDD has not been studied yet and thus is questionable, especially in long-term studies, therefore here we focus on the as-obtained surfaces.

The reversibility of the redox reactions for inner/outer-sphere redox probes was examined based on the values of peak potentials difference of anodic and cathodic peak (ΔE_p) and I_{pA}/I_{pC} ratio of peak currents of anodic/cathodic signal. ΔE_p values are summarized in Table 3, I_{pA}/I_{pC}
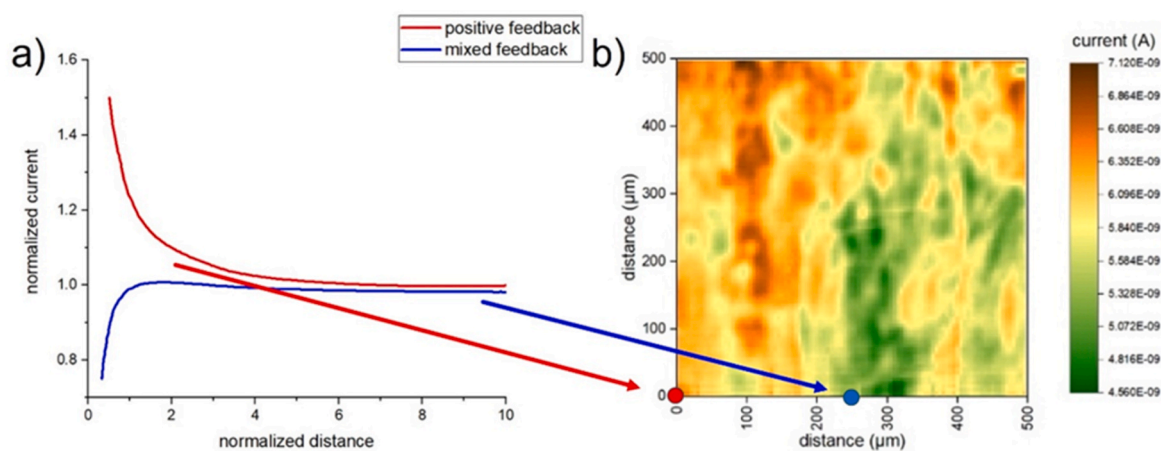

Fig. 4. a) PACs toward the surface of the as-grown BDD$_{8000}$ electrode. Positive (red line) as well as mixed feedback (blue line) was observed during the approach. **b)** SECM image of the as-grown BDD$_{8000}$ electrode with the corresponding positions for the PACs in **a)**. Measurements were conducted in 1.5 mmol L^{-1} FcMeOH in 1 mol L^{-1} KNO$_3$, electrode diameter = 25 μm. Probe potential +0.3 V, quiet time was 15 s. Feedback current of 150% relative to the current in the bulk solution. Arrows and points in red and blue indicate the approach positions corresponding to the feedback behaviour shown in a). (A colour version of this figure can be viewed online.)
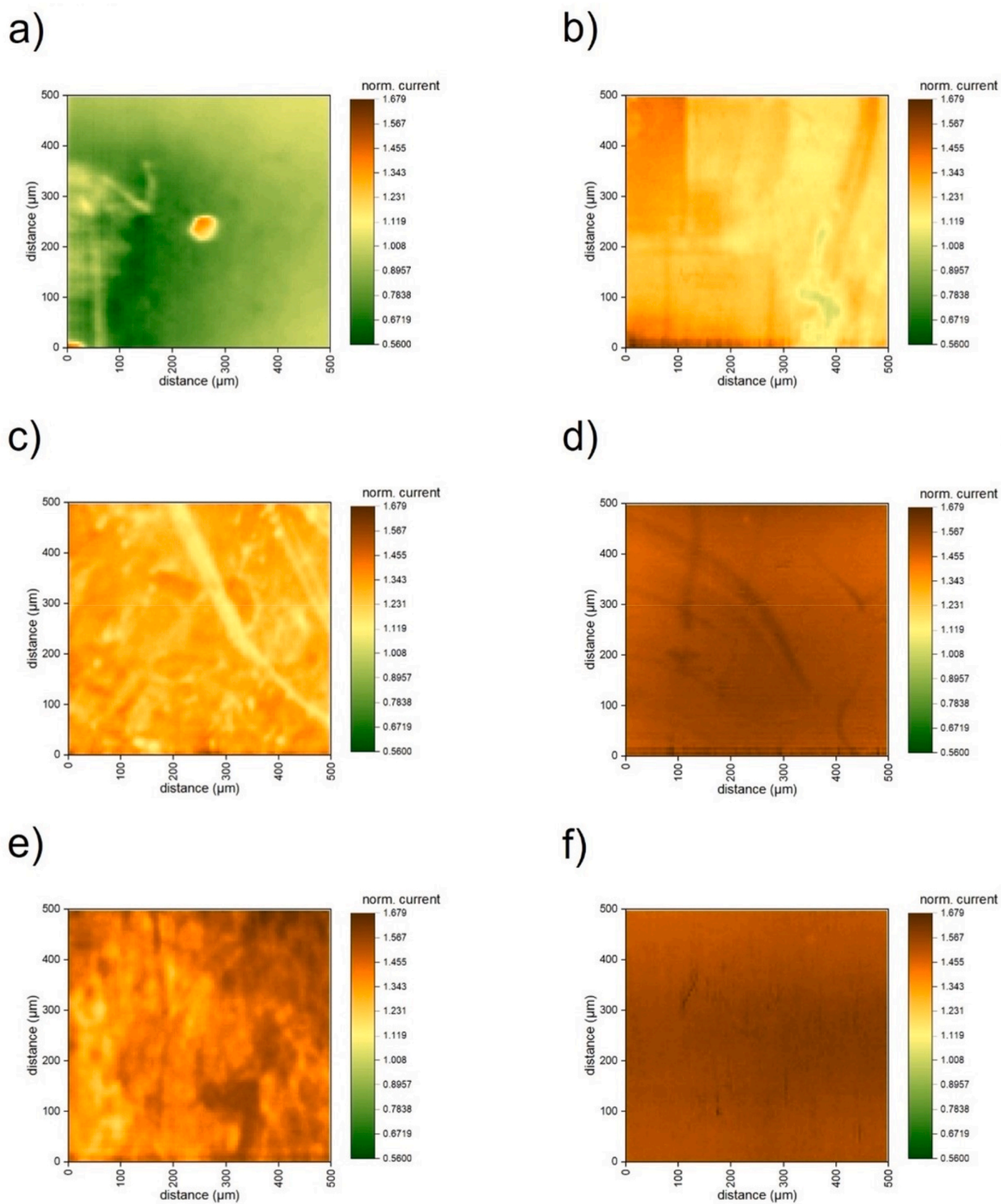
Fig. 5. SECM images of as-grown and CM polished BDD electrodes: a) as-grown BDD_{500}, b) CM polished BDD_{500}, c) as-grown BDD_{2000}, d) CM polished BDD_{2000}, e) as-grown BDD_{8000}, f) CM polished BDD_{8000}. Measurements were conducted in a 1.5 mmol L^{-1} FcMeOH in 1 mol L^{-1} KNO_3, electrode diameter = 25 μm. Probe potential +0.3 V, quiet time was 15 s. Imaging was done at a constant height corresponding to a feedback current of 150% relative to the current in the bulk solution. Current scale was normalized to the bulk current signal. (A colour version of this figure can be viewed online.)

values are listed only for dopamine/dopamine-*o*-quinone (see Table 4) because for other markers they were close to 1.0. Further, values of apparent heterogeneous electron transfer rate constant k_{app}^0 calculated by the Nicholson method from ΔE_p values [36] for all tested inorganic redox markers were estimated and are reported in Table 3.

Fig. 6 represents an example of CV measurements of outer-sphere ($[Ru(NH_3)_6]^{3+/2+}$) and inner-sphere ($[Fe(CN)_6]^{3-/4-}$) probe in 1 mol L^{-1} KCl on all as-grown and CM polished BDD electrodes at a scan rate of 0.1 V s^{-1}. For outer-sphere redox markers reversible or nearly reversible behaviour was observed on all electrodes independent of boron doping level and surface morphology, characterized by ΔE_p values ranging from 60 mV to 71 mV for $[Ru(NH_3)_6]^{3+/2+}$ (CVs in Fig. 6 a), b)) and from 55 mV to 66 mV for $[IrCl_6]^{2-/3-}$. For both markers, CM polishing led to unification of ΔE_p values (difference in ΔE_p only 5 mV among the individual electrodes differing in boron doping level). k_{app}^0 values reflect the minimal differences in ΔE_p and lay within one order of magnitude from 0.201 cm s^{-1} to 0.019 cm s^{-1} for both as-grown and CM polished BDD electrodes.

Obviously, the HET kinetics for outer-sphere redox markers on as-grown and CM polished surface is neither influenced by boron doping level nor on surface morphology and is determined by the electron transfer from the solution species to electrode. This transfer is not hindered by the chemical species terminating the BDD surface, *i.e.*, a slightly higher content of oxygenous groups as shown by XPS measurements. Similar insensitivity was reported in our previous study on as-grown surfaces for BDD layers differing in boron content [48] or deposited in various MW PECVD systems [49]. This confirms sufficient conductivity even for lower doped BDD electrodes thanks to the dominant H-terminated surface and relative low oxygen content, slightly increased after CM polishing. Increased ΔE_p values differing from 59 mV for $[Ru(NH_3)_6]^{3+/2+}$ redox probe were reported for O-terminated surfaces and low boron content in BDD layers deaccelerating HET kinetics [14,16]. Values lower than 59 mV were attributed to increased sp^2 carbon content with attached oxygen functionalities bearing partially negative charge thus supporting adsorption of the positively charged $[Ru(NH_3)_6]^{3+/2+}$ redox marker recognized in porous BDD layers [44] or the effect of thin layer diffusion know from other carbon porous materials [50–52].

However, the changes in HET kinetics due to CM polishing procedure are clearly visible using surface-sensitive inner-sphere redox marker $[Fe(CN)_6]^{3-/4-}$. While ΔE_p values for as-grown BDD electrodes range from 429 mV to 228 mV, CM polished BDD electrodes display substantially

lower values ranging from 100 mV to 75 mV (CVs in Fig. 6 c), d)) and characteristics in Table 3. Fig. S7b) represent the expected decline in ΔE_p values with increasing [B] estimated from Raman. In general, ΔE_p values for $[Fe(CN)_6]^{3-/4-}$ on BDD electrodes increase with increasing oxygen content (due to interaction of the redox marker with π electrons present in oxygenous groups [53]) and decreasing boron content [11,12,48,54]. For the as-grown BDD electrodes, higher values of ΔE_p for $[Fe(CN)_6]^{3-/4-}$ on the lower doped layers indicate a limited number of charge carriers, *i.e.*, boron-rich sites eventually blocked by the presence of oxygenous groups. Clearly CM polishing leads to dramatic acceleration of HET kinetics, which is more pronounced for lower doped BDD electrodes. This might be due to the uniform distribution of boron atoms recognized by uniform electrochemical activity in SECM for BDD$_{500}$ − BDD$_{2000}$ electrodes together with a relative increase in boron concentration on the surface after CM polishing for BDD$_{4000}$ and BDD$_{8000}$, as seen in XPS measurements. The increase in HET kinetics is characterized by k_{app}^0 values from 0.005 cm^2 s^{-1} (500 ppm) to 0.019 cm^2 s^{-1} (8000 ppm) on CM polished surfaces. k_{app}^0 values for $[Fe(CN)_6]^{3-/4-}$ were further evaluated from Tafel plots (depicted in Fig. S8, k_{app}^0 values listed in Table 3) for all as-grown and CM polished BDD electrodes. All evaluated kinetic and thermodynamic parameters are listed in Table S2. E^0 values are ~ +0.273 V for all studied BDD films. Tafel slopes varied around 118 mV per decade for as-grown BDD films, which correlates with a 1e$^-$ process. For CM polished BDD electrodes they range from 105 to 152 mV per decade. This can be explained by accelerated HET kinetics on the CM polished BDD electrodes in comparison with the as-grown ones and therefore complicated and inaccurate evaluation of Tafel slopes. The values of transfer coefficient α and β are around 0.5 which indicates the symmetry of kinetics of the oxidation/reduction reaction. Evaluation of Tafel slopes enables calculation of k_{app}^0 values for all as-grown BDD electrodes even for those with lower boron doping levels (500, 1000 and 2000 ppm), not assessed by Nicholson method. For as-grown BDD films, k_{app}^0 values vary from 0.00044 to 0.00163 cm s^{-1} for BDD$_{500}$ to BDD$_{8000}$, *i.e.*, roughly increase with increasing boron doping level and are comparable with the values of k_{app}^0 calculated by the Nicholson method for BDD$_{4000}$ and BDD$_{8000}$. The values calculated for CM polished electrodes are in general higher, about 0.006 cm s^{-1} for BDD$_{500}$ and BDD$_{1000}$, *i.e.*, comparable with values calculated by Nicholson method. For CM polished electrodes with higher doping level, they increase to 0.0075 cm s^{-1} documenting faster HET kinetics, however these values are lower than that estimated by Nicholson, which can be caused by complicated Tafel slope evaluation as mentioned above. The

Table 3
Calculated ΔE_p and k_{app}^0 values for inorganic redox markers, Y^0 and N values of CPE estimated by EIS in 1 mol L^{-1} KCl at 0 V and R_{ct} estimated by EIS in 1 mmol L^{-1} [Fe(CN)$_6$]$^{3-/4-}$ at +0.25 V on as-grown (AG) and CM polished (CMP) BDD$_{500}$ − BDD$_{8000}$ electrodes.

Cyclic voltammetry							Electrochemical impedance spectroscopy					
Marker	$[Ir(Cl_6)]^{2-/3-}$		$[Ru(NH_3)_6]^{3+/2+}$		$[Fe(CN)_6]^{3-/4-}$		1 mol L^{-1} KCl		1 mmol L^{-1} [Fe(CN)$_6$]$^{3-/4-}$			
	AG	CMP	AG	CMP	AG	CMP	AG	CMP	AG	CMP		
Sample	ΔE_p (mV)						$^b Y^0$	N	$^b Y^0$	N	R_{ct} (kΩ)	R_{ct} (kΩ)
BDD$_{500}$	66	55	71	65	429	100	4.50	0.977	12.0	0.973	278	3.17
BDD$_{1000}$	57	55	63	60	270	100	5.01	0.955	27.1	0.894	52.7	2.7
BDD$_{2000}$	60	60	63	60	297	85	8.05	0.937	17.1	0.963	38.7	1.56
BDD$_{4000}$	63	60	63	60	225	75	14.7	0.936	37.2	0.923	14.7	0.579
BDD$_{8000}$	66	55	69	60	228	75	13.2	0.907	40.8	0.923	14.9	0.45
k_{app}^0 (cm s^{-1})	Nicholson method								Tafel plots for		[Fe(CN)$_6$]$^{3-/4-}$	
BDD$_{500}$	0.040	0.201	0.019	0.041	^{a}_	0.005			0.00046		0.00634	
BDD$_{1000}$	0.201	0.201	0.057	0.164	^{a}_	0.005			0.00137		0.00534	
BDD$_{2000}$	0.201	0.201	0.057	0.164	^{a}_	0.010			0.00107		0.00679	
BDD$_{4000}$	0.071	0.201	0.057	0.164	0.001	0.019			0.00098		0.00710	
BDD$_{8000}$	0.040	0.201	0.022	0.164	0.001	0.019			0.00163		0.00728	

The impedance of the CPE is provided by: $Z_Q = \dfrac{1}{Y_O (j\omega)^n}$

^{a} For ΔE_p values above 212 mV the dimensionless parameter ψ isn't defined thus k_{app}^0 couldn't be calculated.
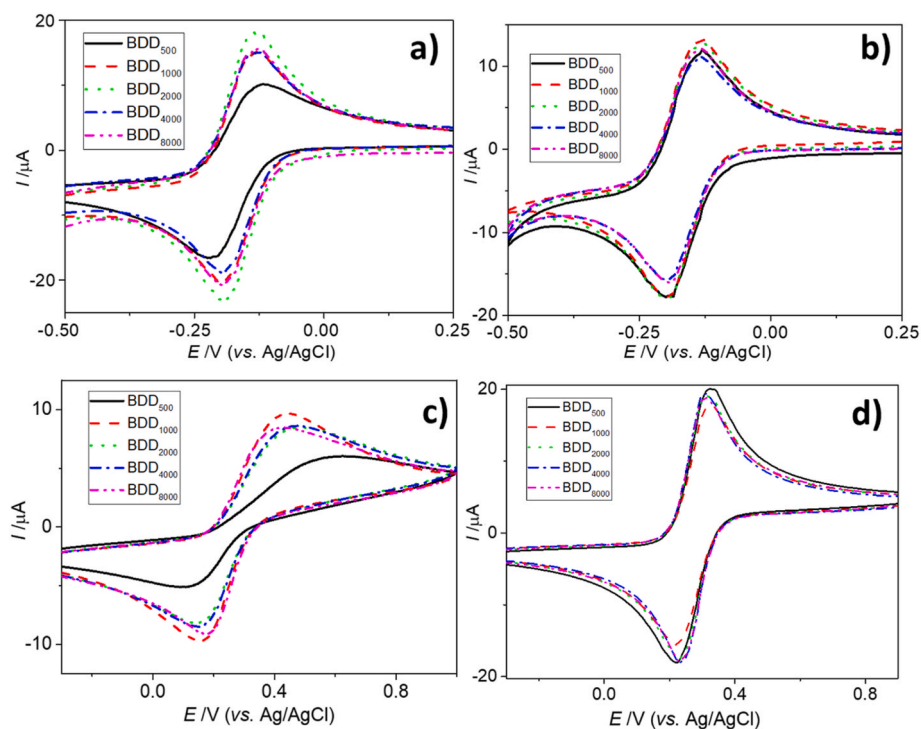^{b} The units of Y^0 values are μMho s^{-1}cm^{-2}.

Fig. 6. Cyclic voltammograms of **a)** 1 mmol L^{-1} [Ru(NH$_3$)$_6$]$^{3+/2+}$ and **c)** 1 mmol L^{-1} [Fe(CN)$_6$]$^{3-/4-}$ on as-grown BDD electrodes, and **b)** 1 mmol L^{-1} [Ru(NH$_3$)$_6$]$^{3+/2+}$, **d)** 1 mmol L^{-1} [Fe(CN)$_6$]$^{3-/4-}$ on CM polished BDD electrodes. Supporting electrolyte 1 mol L^{-1} KCl, scan rate 0.1 V s^{-1}. (A colour version of this figure can be viewed online.)

last method used for calculation of k_{app}^0 is based on evaluation of PAC curves obtained from SECM measurements. When we compare k_{app}^0 values obtained from SECM using [Ru(NH$_3$)$_6$]$^{3+/2+}$ as a redox probe (see Section 3.3) with k_{app}^0 values obtained from CV measurements for BDD$_{4000}$ electrodes using outer and inner sphere probes the same trend can be seen, *i.e.* higher k_{app}^0 values on CM polished in comparison with as-grown BDD surfaces. The absolute k_{app}^0 values evaluated from SECM also show a lower variance for CM polished BDD electrodes confirming lower heterogeneity in electrochemical activity of the surface.

Both methods for evaluation of HET kinetics witness its acceleration for surface sensitive [Fe(CN)$_6$]$^{3-/4}$ due to CM polishing. Clearly, a slight increase in oxygenous groups on CM polished electrodes is not the main factor influencing HET kinetics. The same is valid for the content of non-diamond phase, as shown in Fig. S7a) depicting the dependence of ΔE_p values for redox markers on sp^3/sp^2 evaluated from Raman measurements. Only minor differences in ΔE_p values can be recognized for outer sphere markers and [Fe(CN)$_6$]$^{3-/4-}$. Clearly, CM polished electrodes benefit from the reduction in surface roughness leading to uniform surface conductivity and the other factors (presence of oxygenous groups on the surface, sp^2 carbon content, boron doping level) have minor effect when considering electrochemical behaviour of these redox markers.

Additionally, EIS measurements were performed in 0.1 mol L^{-1} KCl at 0 V to evaluate the effect of boron content and CM polishing on capacitance values. Nyquist plots in the frequency range from 100 000 Hz–0.1 Hz in 1 M KCl are shown in Fig. S9 (with a detail for 100 kHz to 10 Hz in Fig. S10). Data were fitted by the equivalent circuit containing constant phase element (CPE) which is depicted in Fig. S10a). The obtained values of parameter Y^0 (characterizing capacitance of the double layer) and N parameter (characterizing the extent of difference in roughness of the surface) are listed in Table 3. Y^0 values increase with increasing boron content reaching values from 4 500 nMho s^{-1} cm^{-2} to 13 000 nMho s^{-1} cm^{-2} for as-grown BDD$_{500}$ to BDD$_{8000}$ films and from 12 000 nMho s^{-1}cm^{-2} to 40 000 nMho s^{-1}cm^{-2} for CM polished BDD$_{500}$ to BDD$_{8000}$ films, respecting the increasing number of charge transfer

carriers with increasing boron doping level known from other EIS studies on BDD electrodes [48,49,55]. Much higher Y^0 values are observed on the CM polished in comparison with as-grown BDD due to the contribution of a higher number of boron-rich places in BDD films and the uniformity of surface morphology after CM polishing. The increased Y^0 value for CM polished BDD$_{1000}$ electrode documents the presence of residual structure features (Table 3) in comparison with another CM polished BDD electrodes. The N values are getting smaller with increasing boron content in the BDD electrodes. This trend is nicely seen in Fig. S10 of the EIS measurements of KCl where with smaller N values the fitted curve is getting closer to the *x* axis which indicates increasing deviation from the ideal capacitance.

Nyquist plots obtained from EIS measurements of 1 mmol L^{-1} [Fe(CN)$_6$]$^{3-/4-}$ in 1 mol L^{-1} KCl at a potential of $+E = 0.25$ V are depicted in Fig. S11. The R_{ct} values obtained from fitted circuit (inset in Fig. S11a) are listed in Table 3. Obviously, they match with data obtained from cyclic voltammetry. With higher boron content the redox process on BDD electrodes runs easier with regards to the R_{ct} and, obviously, the charge transfer resistances are much lower on the CM polished BDD electrodes in comparison with as-grown BDD electrodes. Again, EIS results demonstrate the superiority of surfaces treated by chem-mechanical polishing in comparison with those without it.

A thorough comparison of as-grown and CM polished electrodes studied in this work with other BDD electrodes can be performed based on the overview of electrochemical parameters in Table S3. BDD electrodes with metallic-type conductivity (*i.e.* [B] $> 2 \times 10^{20}$ cm^{-3} [11]), exhibit in general lower ΔE_p values for [Ru(NH$_3$)$_6$]$^{3+/2+}$ than for [Fe(CN)$_6$]$^{3-/4-}$ in concordance with our study and with the outer sphere character of the former redox probe. The other trend which can be seen are higher ΔE_p values for [Fe(CN)$_6$]$^{3-/4-}$ on O-terminated surfaces in comparison with H-terminated surfaces. However, the extent of hydrogenation/oxidation of the surface is usually not supported by XPS or other data and only the method used for surface treatment is described, which makes comparison of ΔE_p values problematic. ΔE_p values for [Fe(CN)$_6$]$^{3-/4-}$ obtained in our study on CM polished electrodes in the

range from 75 mV to 100 mV are close to 65 mV obtained for BDD alumina polished surface with [B] $\approx 1.9 \times 10^{20}$ cm^{-3} [12] or 114 mV for frequently used commercial BDD electrode (B/C 1000 ppm, formerly Windsor Scientific (UK), now Biologic SAS (France)) [26]. C_{dl} values estimated for various BDD electrodes in Table S3 can be compared with Y^0 values characterizing the capacitance obtained in our study. Values of $C_{dl} < 17.3$ μF cm^{-2} characterize the capacitance of BDD electrodes overviewed in Table S3, and are comparable with Y^0 values for the as-grown set. Higher values of Y^0 for CM polished samples are presumably caused by uniform conductivity of the surface due to smoothing of the surface following CM polishing. Values are close to those obtained on uniform sp^2 carbon surfaces.

3.5. Electrochemical study of dopamine

To further probe and compare the electrochemical performance of as-grown and CM polished BDD electrodes, voltammetric experiments were performed with a more complex organic redox couple structure, dopamine/dopamine-*o*-quinone, in 0.1 mol L^{-1} phosphate buffer pH 7.4. Dopamine was selected as its redox reaction is well-defined (in pH $\sim$ 7 involves exchange of 2 H$^+$ and 2 e^- [56]; dopamine is positively charged at this pH (pK_a = 8.93) [57]. It proceeds through inner-sphere electron transfer, which makes dopamine very sensitive to the surface and electronic characteristics of the BDD electrodes. This sensitivity can be clearly recognized by differences in ΔE_p values due to changes of HET kinetics for the quasireversible dopamine redox system, being dependent on surface termination [20,49,58–60], sp^2 carbon impurities [20,61], and boron content [48].

3.5.1. Cyclic voltammetry

Cyclic voltammograms recorded in dopamine solution (1 mmol L^{-1}) in the potential range from -0.5 V to $+1.5$ V on all studied electrodes are depicted in Fig. 7 and valuable parameters extracted from these measurements are summarized in Table 4.

On as-grown BDD electrodes, a trend in the shift of the anodic peak potential (E_{pA}), corresponding to dopamine oxidation, toward lower potential values with increasing boron doping can be clearly identified (Fig. 7a); specifically, a dramatic difference of $\sim$430 mV was recognized in E_{pA} between as-grown BDD$_{500}$ and BDD$_{8000}$ electrodes. In addition, only on electrodes prepared at higher B/C, i.e., BDD$_{4000}$ and BDD$_{8000}$, a small cathodic peak, ascribed to reduction of dopamine-*o*-quinone back to dopamine, was recognized at a potential of $\sim$0 V (see inset in Fig. 7a). Hence, dopamine redox reaction exhibits the fully irreversible nature on as-grown BDD electrodes deposited at lower B/C ($\leq$2000 ppm). As can be further seen in Fig. 7a, the intensity of oxidation peak current (I_{pA}) gradually increased with an increase in B/C and the I_{pA} recorded on as-grown BDD$_{8000}$ almost doubled, compared to BDD$_{500}$. The observed phenomena can be ascribed to the higher doping levels and thus higher conductivity facilitating dopamine/dopamine-*o*-quinone redox reactions [48], but also to the presence of sp^2 carbon impurities, whose increased content was confirmed in as-grown BDD$_{4000}$ and BDD$_{8000}$ by

Raman spectroscopy (see Fig. S2). The impact of sp^2-bonded carbon presumably results from the synergic effect of its electrocatalytic and adsorption-promoting role, while the latter may cause, to some extent, 'preconcentration' of dopamine molecules or oxidation product(s) on the BDD surface [20,48].

Similar trends, i.e., a decrease in E_{pA} along with an increase in I_{pA} with boron content was observed on CM polished BDD electrodes (see Fig. 7b), however, both trends were significantly less pronounced in comparison with as-grown electrodes. Specifically, (i) a shift in E_{pA} occurred within a much narrower potential range (from +558 mV to +408 mV) and E_{pA} even remained constant for electrodes with B/C $\geq$ 2000 ppm, and (ii) a difference in the I_{pA} intensity of only $\sim$17% between CM polished BDD$_{500}$ and BDD$_{8000}$ was discerned. In contrast to as-grown electrodes, a cathodic peak is clearly developed on all CM polished BDD electrodes, as shown in the inset in Fig. 7b, indicating the increased reversible behaviour of the dopamine/dopamine-*o*-quinone redox system. Importantly, parameters characterizing 'reversibility', ΔE_p and $|I_{pA}/I_{pC}|$ ratio (Table 4), improved with increased doping levels. Lower ΔE_p values, and thus faster HET kinetics, were recognized on CM polished BDD of higher B/C $\geq$ 2000 ppm which is related to the greater content of electroactive sites, i.e., boron atoms and sp^2 carbon spots, accelerating dopamine redox reaction. It has been previously postulated that the more sp^2 carbon present on the BDD surface, the larger the dopamine adsorption is, which consequently manifests in a smaller ΔE_p [61]. Obviously HET kinetics of dopamine is more sensitive to boron doping level and sp^2 carbon content being accelerated with their increase, than HET kinetics of Fe(CN)$_6^{3-/4-}$. Naturally, HET kinetics benefits from the uniformity of the CM polished surfaces as confirmed for the other redox markers.

Finally, as can be seen in Table 4, the differences between as-grown and CM polished electrodes are more evident at lower B/C, while with an increase in the content of boron dopant and sp^2 carbon sites, differences gradually diminish resulting in much more comparable dopamine responses, most visibly on BDD$_{8000}$, regardless of the surface microstructure (as-grown vs. CM polished).

3.5.2. Square-wave voltammetry

Clearly, CV experiments revealed the enhanced electrochemical performance of CM polished BDD electrodes. To verify that such a significant boost also translates into improved analytical parameters essential for the development of electrochemical sensors, further voltammetric experiments were performed with as-grown and CM polished BDD$_{500}$ and BDD$_{4000}$ electrodes. These four electrodes were selected to act as representatives of electrodes with lower and higher boron and sp^2 carbon content, and simultaneously they reflect either more or less pronounced differences among the two sets. Specifically, a well-established and sensitive SWV technique with previously optimized parameters (overviewed in Section 2.3 for each electrode) was employed to record concentration dependences of dopamine (Fig. S12). The obtained analytical parameters, i.e., linear dynamic range (LDR) and calculated LOD values, using the procedure described in Section 2.3, for all four BDD electrodes are reported in Table 5.

The widest LDR providing linear current responses for the entire range of dopamine concentrations (from 1.0 to 100.0 μmol L^{-1}) was only obtained on the CM polished BDD$_{4000}$ electrode, whereas a break in the linear range occurred on the other three studied electrodes (see Fig. S12). Similarly, two LDR within the investigated concentration range have been recognized in previous studies on catecholamine neurotransmitters, dopamine [49,62] and epinephrine [63], and their metabolite vanillylmandelic acid [64]. Further, assessing both sets individually, higher doped BDD$_{4000}$ electrodes provided lower *LOD* values, compared to BDD$_{500}$ electrodes. Nevertheless, when the two sets are compared, CM polished electrodes certainly outperform both as-grown BDD electrodes, i.e., even CM polished BDD$_{500}$ exhibits better electroanalytical characteristics than as-grown BDD$_{4000}$ (see Table 4). Overall, the lowest *LOD* of 0.23 μmol L^{-1} and the highest sensitivity was achieved on CM polished
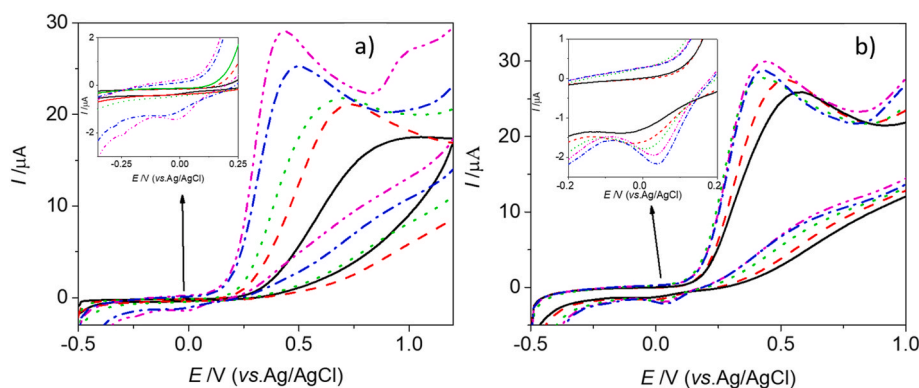
Table 4
Parameters extracted from CVs recorded on as-grown and CM polished BDD electrodes characterizing dopamine/dopamine-o-quinone redox reaction: dopamine oxidation potential (E_{pA}), the peak-to-peak separation (ΔE_p), and the ratio of anodic and cathodic peak currents $|I_{pA}/I_{pC}|$.

Sample	as-grown	CM polished	as-grown	CM polished	as-grown	CM polished
	E_{pA} (mV)		ΔE_p (mV)		$|I_{pA}/I_{pC}|$	
BDD$_{500}$	+840	+558	[a]_	501	[a]_	18.5
BDD$_{1000}$	+699	+480	[a]_	423	[a]_	16.8
BDD$_{2000}$	+537	+410	[a]_	353	[a]_	15.4
BDD$_{4000}$	+459	+408	447	351	19.4	14.9
BDD$_{8000}$	+414	+408	384	351	20.2	13.7

[a] Values are not reported, as cathodic peak is absent in the recorded CVs.

Fig. 7. CVs of 1 mmol L^{-1} dopamine in 0.1 mol L^{-1} phosphate buffer pH 7.4 recorded on (**A**) as-grown BDD and (**B**) CM polished BDD electrodes: (——) BDD$_{500}$, (— —) BDD$_{1000}$, (• • •) BDD$_{2000}$, (– • –) BDD$_{4000}$, and (– • •) BDD$_{8000}$, using a scan rate of 0.1 V s^{-1}. (A colour version of this figure can be viewed online.)

Table 5
Analytical parameters of concentration dependences of dopamine in 0.1 mol L^{-1} phosphate buffer of pH 7.4 obtained by SWV using optimized parameters, with calculated *LOD* values.

BDD electrode	LDR	Slope	Intercept	R	LOD
	(µmol L^{-1})	(nA µmol L^{-1})	(nmol L^{-1})		(µmol L^{-1})
As-grown					
BDD$_{500}$	6.0–20.0	4.9 ± 0.4	−0.020 ± 0.003	0.9899	1.82
	20.0–100.0	11.8 ± 0.7	−0.133 ± 0.032	0.9931	
BDD$_{4000}$	2.0–10.0	3.7 ± 0.2	−0.004 ± 0.001	0.9940	1.06
	10.0–80.0	6.8 ± 0.2	−0.044 ± 0.006	0.9984	
CM polished					
BDD$_{500}$	4.0–10.0	3.6 ± 0.2	−0.008 ± 0.001	0.9964	0.84
	10.0–80.0	11.2 ± 0.4	−0.086 ± 0.006	0.9976	
BDD$_{4000}$	1.0–100.0	52.6 ± 1.1	−0.020 ± 0.004	0.9987	0.23

BDD$_{4000}$. Apparently, smoother surfaces with larger areas of exposed and thus available electroactive sites including boron atoms and sp^2 carbon domains, whose effects were thoroughly discussed above, contribute to the superior electroanalytical performance of CM polished BDD electrodes. The achieved submicromolar *LOD*s and LDR over two orders of magnitude for the CM polished BDD$_{4000}$ electrode is comparable with analytical figures of merit obtained on other non-modified O- and H-terminated BDD electrodes as can be seen from the overview of their analytical performance in Table S4.

4. Conclusion

A thorough experimental study was performed with a set of ultra-thin (≤500 nm) BDD layers deposited at B/C ratios 500 ppm–8000 ppm aiming at comparison of as-grown polycrystalline and CM polished electrodes.

The main effects of the CM polishing can be summarized as follows:

(i) The CM polished electrode (BDD$_{2000}$) exhibits a strong texture with component in the {011} and {111} orientation, confirmed by EBSD measurements.

(ii) Raman spectroscopy revealed an increase in sp^2 carbon content in BDD$_{4000}$ and BDD$_{8000}$ electrodes in comparison with lower doped BDD$_{500-2000}$ electrodes, and importantly, CM polishing did not cause any increase in amount of sp^2 carbon impurities (regarding sensitivity of Raman measurements).

(iii) XPS revealed the higher surface quality of CM polished BDD layers, only a minor rise in oxygen content and an increase in boron content for BDD$_{4000}$ and BDD$_{8000}$ electrodes in comparison with as-grown layers. This effect can be explained by CM polishing exposing boron atoms present in bulk of the BDD, where the concentration is higher than on the surface due to a "shutdown" effect during the switch off procedure following CVD

leading to diamond deposition with lower [B] content due to changes in the final deposition conditions.

(iv) SECM using FcMeOH as a redox probe proved that the conductivity of as-grown BDD layers is heterogeneously distributed, as-grown surfaces possess spots of high electrochemical activity as well as insulating spots (the latter increases with decreasing boron content). CM polished BDD electrodes exhibit better uniform distribution of surface activity, especially for highly doped BDD, in agreement with uniform distribution of boron atoms in the bulk of BDD layers [43–45].

(v) The increase in Y^0 values characterizing the capacitance with increasing boron content estimated by EIS is presumably caused by an increasing number of charge carriers, represented by boron atoms and sp^2 carbon in BDD$_{4000}$ and BDD$_{8000}$ layers. The higher values of Y^0 and lower values of charge transfer resistance R_{ct} of CM polished in comparison with as-grown layers can be assigned to increased surface boron concentration in BDD$_{4000}$ and BDD$_{8000}$ layers, confirmed by XPS and uniform conductivity of the surface due to smoothing of the surface imposed by polishing.

(vi) The HET kinetics of outer-sphere redox markers ([IrCl$_6$]$^{2-/3-}$ and [Ru(NH$_3$)$_6$]$^{3+/2+}$) sphere is (nearly) reversible, independent on boron doping level and surface morphology. The HET kinetics of inner-sphere redox markers ([Fe(CN)$_6$]$^{3-/4-}$, dopamine/dopamine-*o*-quinone) is accelerating with increasing boron doping level, as recognized by decreased ΔE_p values. A significant enhancement of HET kinetics (more pronounced for lowly doped films) has been recognized on CM polished BDD electrodes. For Fe(CN)$_6$$^{3-/4-}$, the slightly higher amount of oxygenous groups on the CM polished surface, sp^2 carbon content, and boron doping level have minor effect and the HET kinetics accelerates due to reduction in surface roughness leading to uniform surface conductivity. The HET kinetics of dopamine is more sensitive to

boron doping level and sp^2 carbon content being accelerated with their increase.

(vii) Electroanalytical characteristics estimated for dopamine in phosphate buffer revealed that BDD$_{500}$ and BDD$_{4000}$ CM polished electrodes outperform BDD$_{500}$ and BDD$_{4000}$ as-grown electrodes. The lowest *LOD* of 0.23 μmol L^{-1}, the widest linear dynamic range and the highest sensitivity was achieved on CM polished BDD$_{4000}$ electrode.

Obviously, the changes in electrochemical characteristics described in (iv) – (vii) reveal that CM polished BDD electrodes possess uniform distribution of conductivity due to smoothing of the surface as proved by scanning electrochemical microscopy, faster heterogenous electron transfer kinetics for inner-sphere redox markers ([Fe(CN)$_6$]$^{3-/4-}$ and dopamine) and higher values of double layer capacitance. However, CM polished surfaces presumably contain uniformly distributed charge carriers as a result of continuous BDD growth during the unaltered CVD process, moreover on a relatively smooth surface with less grain boundary influence. This homogeneity of CM polished surfaces is obviously the key parameter for boosting the electrochemical and electroanalytical characteristics. The other major effect influencing electrochemical properties includes increased number of charge carriers, represented by boron atoms, and eventually sp^2 carbon in BDD$_{4000}$ and BDD$_{8000}$ films.

To conclude, CM polishing or other advanced diamond polishing methods [32] seem to be a very effective way for altering the electrochemical properties of BDD. Further studies are needed to evaluate their fouling resistivity, efficacy in productivity of hydroxyl radicals, possibilities of local surface structuring, and surface termination to extend their possibilities in (bio)sensing, incineration of organic compounds and electrocatalytic applications.

CRediT authorship contribution statement

M. Zelenský: Writing – original draft, Investigation, Visualization. **J. Fischer:** Methodology, Funding acquisition. **S. Baluchová:** Investigation, Visualization. **L. Klimša:** Investigation, Visualization. **J. Kopeček:** Investigation. **M. Vondráček:** Investigation, Visualization. **L. Fekete:** Investigation, Visualization. **J. Eidenschink:** Investigation, Visualization. **F.-M. Matysik:** Investigation, Supervision. **S. Mandal:** Investigation. **O.A. Williams:** Investigation. **M. Hromadová:** Investigation. **V. Mortet:** Conceptualization. **K. Schwarzová-Peccová:** Writing – review & editing, Conceptualization, Supervision. **A. Taylor:** Writing – review & editing, Investigation, Funding acquisition.

Declaration of competing interest

The authors declare that they have no known competing financial interests or personal relationships that could have appeared to influence the work reported in this paper.

Data availability

Data will be made available on request.

Acknowledgements

Appendix A. Supplementary data

Supplementary data to this article can be found online at https://doi.org/10.1016/j.carbon.2022.11.069.

References

[1] K. Muzyka, J. Sun, T.H. Fereja, Y. Lan, W. Zhang, G. Xu, Boron-doped diamond: current progress and challenges in view of electroanalytical applications, Anal. Methods 11 (2019) 397–414, https://doi.org/10.1039/C8AY02197J.

[2] B.C. Lourencao, R.F. Brocenschi, R.A. Medeiros, O. Fatibello-Filho, R.C. Rocha-Filho, Analytical applications of electrochemically pretreated boron-doped diamond electrodes, Chemelectrochem 7 (2020) 1291–1311, https://doi.org/10.1002/celc.202000050.

[3] N. Yang, S. Yu, J.V. Macpherson, Y. Einaga, H. Zhao, G. Zhao, G.M. Swain, X. Jiang, Conductive diamond: synthesis, properties, and electrochemical applications, Chem. Soc. Rev. 48 (2019) 157–204, https://doi.org/10.1039/C7CS00757D.

[4] S. Baluchová, A. Daňhel, H. Dejmková, V. Ostatná, M. Fojta, K. Schwarzová-Peccová, Recent progress in the applications of boron doped diamond electrodes in electroanalysis of organic compounds and biomolecules – a review, Anal. Chim. Acta 1077 (2019) 30–66, https://doi.org/10.1016/j.aca.2019.05.041.

[5] R.F. Brocenschi, P. Hammer, C. Deslouis, R.C. Rocha-Filho, Assessments of the effect of increasingly severe cathodic pretreatments on the electrochemical activity of polycrystalline boron-doped diamond electrodes, Anal. Chem. 88 (2016) 5363–5368, https://doi.org/10.1021/acs.analchem.6b00676.

[6] J.V. Macpherson, A practical guide to using boron doped diamond in electrochemical research, Phys. Chem. Chem. Phys. 17 (2015) 2935–2949, https://doi.org/10.1039/C4CP04022H.

[7] S. Garcia-Segura, E. Vieira dos Santos, C.A. Martínez-Huitle, Role of sp3/sp2 ratio on the electrocatalytic properties of boron-doped diamond electrodes: a mini review, Electrochem. Commun. 59 (2015) 52–55, https://doi.org/10.1016/j.elecom.2015.07.002.

[8] Y. Einaga, J.S. Foord, G.M. Swain, Diamond electrodes: diversity and maturity, MRS Bull. 39 (2014) 525–532, https://doi.org/10.1557/mrs.2014.94.

[9] J. Ryl, A. Zielinski, L. Burczyk, R. Bogdanowicz, T. Ossowski, K. Darowicki, Chemical-assisted mechanical lapping of thin boron-doped diamond films: a fast route toward high electrochemical performance for sensing devices, Electrochim. Acta 242 (2017) 268–279, https://doi.org/10.1016/j.electacta.2017.05.027.

[10] M. Bernard, C. Baron, A. Deneuville, About the origin of the low wave number structures of the Raman spectra of heavily boron doped diamond films, Diam. Relat. Mater. 13 (2004) 896–899, https://doi.org/10.1016/j.diamond.2003.11.082.

[11] K. Schwarzová-Peccová, J. Vosáhlová, J. Barek, I. Šloufová, E. Pavlova, V. Petrák, J. Zavázalová, Influence of boron content on the morphological, spectral, and electroanalytical characteristics of anodically oxidized boron-doped diamond electrodes, Electrochim. Acta 243 (2017) 170–182, https://doi.org/10.1016/j.electacta.2017.05.006.

[12] L.A. Hutton, J.G. Iacobini, E. Bitziou, R.B. Channon, M.E. Newton, J. V. Macpherson, Examination of the factors affecting the electrochemical performance of oxygen-terminated polycrystalline boron-doped diamond electrodes, Anal. Chem. 85 (2013) 7230–7240, https://doi.org/10.1021/ac401042t.

[13] A.W.S. Williams, E.C. Lightowlers, A.T. Collins, Impurity conduction in synthetic semiconducting diamond, J. Phys. C Solid State Phys. 3 (1970) 1727–1735, https://doi.org/10.1088/0022-3719/3/8/011.

[14] R. Šelešovská, B. Kränková, M. Štěpánková, P. Martinková, L. Janíková, J. Chýlková, M. Vojs, Influence of boron content on electrochemical properties of boron-doped diamond electrodes and their utilization for leucovorin determination, J. Electroanal. Chem. 821 (2018) 2–9, https://doi.org/10.1016/j.jelechem.2018.02.007.

[15] A.N. Ndao, F. Zenia, A. Deneuville, M. Bernard, C. Lévy-Clément, Effect of boron concentration on the electrochemical reduction of nitrates on polycrystalline diamond electrodes, Diam. Relat. Mater. 9 (2000) 1175–1180, https://doi.org/10.1016/S0925-9635(99)00328-3.

[16] Y. Feng, J. Lv, J. Liu, N. Gao, H. Peng, Y. Chen, Influence of boron concentration on growth characteristic and electro-catalytic performance of boron-doped diamond electrodes prepared by direct current plasma chemical vapor deposition, Appl. Surf. Sci. 257 (2011) 3433–3439, https://doi.org/10.1016/j.apsusc.2010.11.041.

[17] J. Li, C.L. Bentley, S. Tan, V.S.S. Mosali, M.A. Rahman, S.J. Cobb, S.-X. Guo, J. V. Macpherson, P.R. Unwin, A.M. Bond, J. Zhang, Impact of sp^2 carbon edge effects on the electron-transfer kinetics of the ferrocene/ferricenium process at a boron-doped diamond electrode in an ionic liquid, J. Phys. Chem. C 123 (2019) 17397–17406, https://doi.org/10.1021/acs.jpcc.9b04519.

[18] J.A. Bennett, J. Wang, Y. Show, G.M. Swain, Effect of sp2-bonded nondiamond carbon impurity on the response of boron-doped polycrystalline diamond thin-film electrodes, J. Electrochem. Soc.. (n.d.) 9.

[19] I. Duo, A. Fujishima, C. Comninellis, Electron transfer kinetics on composite diamond (sp3)–graphite (sp2) electrodes, Electrochem. Commun. 5 (2003) 695–700, https://doi.org/10.1016/S1388-2481(03)00169-3.

[20] T. Watanabe, Y. Honda, K. Kanda, Y. Einaga, Tailored design of boron-doped diamond electrodes for various electrochemical applications with boron-doping level and sp^2-bonded carbon impurities: tailored design of boron-doped diamond electrodes, Phys. Status Solidi 211 (2014) 2709–2717, https://doi.org/10.1002/pssa.201431455.

[21] S.C.B. Oliveira, A.M. Oliveira-Brett, Voltammetric and electrochemical impedance spectroscopy characterization of a cathodic and anodic pre-treated boron doped diamond electrode, Electrochim. Acta 55 (2010) 4599–4605, https://doi.org/10.1016/j.electacta.2010.03.016.

[22] V. Rehacek, I. Hotovy, M. Marton, M. Mikolasek, P. Michniak, A. Vincze, A. Kromka, M. Vojs, Voltammetric characterization of boron-doped diamond electrodes for electroanalytical applications, J. Electroanal. Chem. 862 (2020), 114020, https://doi.org/10.1016/j.jelechem.2020.114020.

[23] H.B. Suffredini, V.A. Pedrosa, L. Codognoto, S.A.S. Machado, R.C. Rocha-Filho, L. A. Avaca, Enhanced electrochemical response of boron-doped diamond electrodes brought on by a cathodic surface pre-treatment, Electrochim. Acta 49 (2004) 4021–4026, https://doi.org/10.1016/j.electacta.2004.01.082.

[24] Z.V. Živcová, V. Petrák, O. Frank, L. Kavan, Electrochemical impedance spectroscopy of polycrystalline boron doped diamond layers with hydrogen and oxygen terminated surface, Diam. Relat. Mater. 55 (2015) 70–76, https://doi.org/10.1016/j.diamond.2015.03.002.

[25] F. Marken, C.A. Paddon, D. Asogan, Direct cytochrome c electrochemistry at boron-doped diamond electrodes, Electrochem. Commun. 4 (2002) 62–66, https://doi.org/10.1016/S1388-2481(01)00272-7.

[26] J. Zavazalova, K. Prochazkova, K. Schwarzova-Peckova, Boron-doped diamond electrodes for voltammetric determination of benzophenone-3, Anal. Lett. 49 (2016) 80–91, https://doi.org/10.1080/00032719.2014.1003425.

[27] J. Klouda, K. Nesměrák, P. Kočovský, J. Barek, K. Schwarzová-Pecková, A novel voltammetric approach to the detection of primary bile acids in serum samples, Bioelectrochemistry Amst. Neth. 134 (2020), 107539, https://doi.org/10.1016/j.bioelechem.2020.107539.

[28] E.L.H. Thomas, G.W. Nelson, S. Mandal, J.S. Foord, O.A. Williams, Chemical mechanical polishing of thin film diamond, Carbon 68 (2014) 473–479, https://doi.org/10.1016/j.carbon.2013.11.023.

[29] E.L.H. Thomas, S. Mandal, E.B. Brousseau, O.A. Williams, Silica based polishing of 100 and 111 single crystal diamond, Sci. Technol. Adv. Mater. 15 (2014), 035013, https://doi.org/10.1088/1468-6996/15/3/035013.

[30] A. Peguiron, G. Moras, M. Walter, H. Uetsuka, L. Pastewka, M. Moseler, Activation and mechanochemical breaking of C–C bonds initiate wear of diamond (110) surfaces in contact with silica, Carbon 98 (2016) 474–483, https://doi.org/10.1016/j.carbon.2015.10.098.

[31] G.M. Klemencic, S. Mandal, J.M. Werrell, S.R. Giblin, O.A. Williams, Superconductivity in planarised nanocrystalline diamond films, Sci. Technol. Adv. Mater. 18 (2017) 239–244, https://doi.org/10.1080/14686996.2017.1286223.

[32] C. Xiao, F.-C. Hsia, A. Sutton-Cook, B. Weber, S. Franklin, Polishing of polycrystalline diamond using synergies between chemical and mechanical inputs: a review of mechanisms and processes, Carbon 196 (2022) 29–48, https://doi.org/10.1016/j.carbon.2022.04.028.

[33] F. Silva, A. Gicquel, A. Tardieu, P. Cledat, Th Chauveau, Control of an MPACVD reactor for polycrystalline textured diamond films synthesis: role of microwave power density, Diam. Relat. Mater. 5 (1996) 338–344, https://doi.org/10.1016/0925-9635(95)00428-9.

[34] C. Wei, A.J. Bard, M.V. Mirkin, Scanning electrochemical microscopy. 31. Application of SECM to the study of charge transfer processes at the liquid/liquid interface, J. Phys. Chem. A 99 (1995) 16033–16042, https://doi.org/10.1021/j100043a050.

[35] Y. Wang, J. Lin, R. Zong, J. He, Y. Zhu, Enhanced photoelectric catalytic degradation of methylene blue via TiO2 nanotube arrays hybridized with graphite-like carbon, J. Mol. Catal. Chem. 349 (2011) 13–19, https://doi.org/10.1016/j.molcata.2011.08.020.

[36] R.S. Nicholson, Theory and application of cyclic voltammetry for measurement of electrode reaction kinetics, Anal. Chem. 37 (1965) 1351–1355, https://doi.org/10.1021/ac60230a016.

[37] A.J. Bard, L.R. Faulkner, in: Electrochemical Methods: Fundamentals and Applications, second ed., Wiley, New York, 2001.

[38] J.J. Watkins, H.S. White, The role of the electrical double layer and ion pairing on the electrochemical oxidation of hexachloroiridate(III) at Pt electrodes of nanometer dimensions, Langmuir 20 (2004) 5474–5483, https://doi.org/10.1021/la0496993.

[39] J.A.N. Gonçalves, G.M. Sandonato, K. Iha, Characterization of boron doped CVD diamond films by Raman spectroscopy and X-ray diffractometry, Diam. Relat. Mater. 11 (2002) 1578–1583, https://doi.org/10.1016/S0925-9635(02)00103-6.

[40] V. Mortet, Z.V. Živcová, A. Taylor, M. Davydová, O. Frank, P. Hubík, J. Lorincik, M. Aleshin, Determination of atomic boron concentration in heavily boron-doped diamond by Raman spectroscopy, Diam. Relat. Mater. 93 (2019) 54–58, https://doi.org/10.1016/j.diamond.2019.01.028.

[41] V. Mortet, Z. Vlčková Živcová, A. Taylor, O. Frank, P. Hubík, D. Trémouilles, F. Jomard, J. Barjon, L. Kavan, Insight into boron-doped diamond Raman spectra characteristic features, Carbo 115 (2017) 279–284, https://doi.org/10.1016/j.carbon.2017.01.022.

[42] S. Ferro, M. Dal Colle, A. De Battisti, Chemical surface characterization of electrochemically and thermally oxidized boron-doped diamond film electrodes, Carbon 43 (2005) 1191–1203, https://doi.org/10.1016/j.carbon.2004.12.012.

[43] F. Jia, Y. Bai, F. Qu, J. Zhao, C. Zhuang, X. Jiang, Effect of B/C ratio on the physical properties of highly boron-doped diamond films, Vacuum 84 (2010) 930–934, https://doi.org/10.1016/j.vacuum.2010.01.003.

[44] A.F. Azevedo, F.A. Souza, P. Hammer, M.R. Baldan, N.G. Ferreira, The influence of hydrogen plasma pre-treatment on the structure of BDND electrode surface applied

[45] for phenol detection, J. Nanoparticle Res. 13 (2011) 6133–6139, https://doi.org/10.1007/s11051-011-0501-1.

[45] P. Ashcheulov, A. Taylor, Z. Vlčková Živcová, P. Hubík, J. Honolka, M. Vondráček, M. Remzová, J. Kopeček, L. Klimša, J. Lorinčik, M. Davydova, Z. Remeš, M. Kohout, A.M. Beltran, V. Mortet, Low temperature synthesis of transparent conductive boron doped diamond films for optoelectronic applications: role of hydrogen on the electrical properties, Appl. Mater. Today 19 (2020), 100633, https://doi.org/10.1016/j.apmt.2020.100633.

[46] J.I.B. Wilson, J.S. Walton, G. Beamson, Analysis of chemical vapour deposited diamond films by X-ray photoelectron spectroscopy, J. Electron. Spectrosc. Relat. Phenom. 121 (2001) 183–201, https://doi.org/10.1016/S0368-2048(01)00334-6.

[47] P. Kuang, K. Natsui, C. Feng, Y. Einaga, Electrochemical reduction of nitrate on boron-doped diamond electrodes: effects of surface termination and boron-doping level, Chemosphere 251 (2020), 126364, https://doi.org/10.1016/j.chemosphere.2020.126364.

[48] S. Baluchová, A. Taylor, V. Mortet, S. Sedláková, L. Klimša, J. Kopeček, O. Hák, K. Schwarzová-Pecková, Porous boron doped diamond for dopamine sensing: effect of boron doping level on morphology and electrochemical performance, Electrochim. Acta 327 (2019), 135025, https://doi.org/10.1016/j.electacta.2019.135025.

[49] M. Brycht, S. Baluchová, A. Taylor, V. Mortet, S. Sedláková, L. Klimša, J. Kopeček, K. Schwarzová-Pecková, Comparison of electrochemical performance of various boron-doped diamond electrodes: dopamine sensing in biomimicking media used for cell cultivation, Bioelectrochemistry 137 (2021), 107646, https://doi.org/10.1016/j.bioelechem.2020.107646.

[50] S. Sainio, T. Palomäki, S. Rhode, M. Kauppila, O. Pitkänen, T. Selkälä, G. Toth, M. Moram, K. Kordas, J. Koskinen, T. Laurila, Carbon nanotube (CNT) forest grown on diamond-like carbon (DLC) thin films significantly improves electrochemical sensitivity and selectivity towards dopamine, Sensor. Actuator. B Chem. 211 (2015) 177–186, https://doi.org/10.1016/j.snb.2015.01.059.

[51] G.P. Keeley, M.E.G. Lyons, The effects of thin layer diffusion at glassy carbon electrodes modified with porous films of single-walled carbon nanotubes, Int. J. Electrochem. Sci. 4 (2009) 794–809.

[52] I. Streeter, G.G. Wildgoose, L. Shao, R.G. Compton, Cyclic voltammetry on electrode surfaces covered with porous layers: an analysis of electron transfer kinetics at single-walled carbon nanotube modified electrodes, Sensor. Actuator. B Chem. 133 (2008) 462–466, https://doi.org/10.1016/j.snb.2008.03.015.

[53] R.L. McCreery, Advanced carbon electrode materials for molecular electrochemistry, Chem. Rev. 108 (2008) 2646–2687, https://doi.org/10.1021/cr068076m.

[54] K.B. Holt, A.J. Bard, Y. Show, G.M. Swain, Scanning electrochemical microscopy and conductive probe atomic force microscopy studies of hydrogen-terminated boron-doped diamond electrodes with different doping levels, J. Phys. Chem. B 108 (2004) 15117–15127, https://doi.org/10.1021/jp048222x.

[55] T. Watanabe, T.K. Shimizu, Y. Tateyama, Y. Kim, M. Kawai, Y. Einaga, Giant electric double-layer capacitance of heavily boron-doped diamond electrode, Diam. Relat. Mater. 19 (2010) 772–777, https://doi.org/10.1016/j.diamond.2010.02.022.

[56] A.N. Patel, S. Tan, T.S. Miller, J.V. Macpherson, P.R. Unwin, Comparison and reappraisal of carbon electrodes for the voltammetric detection of dopamine, Anal. Chem. 85 (2013) 11755–11764, https://doi.org/10.1021/ac401969q.

[57] https://pubchem.ncbi.nlm.nih.gov/compound/681. (Accessed 11 November 2022).

[58] R. Trouillon, D. O'Hare, Y. Einaga, Effect of the doping level on the biological stability of hydrogenated boron doped diamond electrodes, Phys. Chem. Chem. Phys. 13 (2011) 5422–5429, https://doi.org/10.1039/C0CP02420A.

[59] Z. Liu, S. Baluchová, A.F. Sartori, Z. Li, Y. Gonzalez-Garcia, M. Schreck, J. G. Buijnsters, Heavily boron-doped diamond grown on scalable heteroepitaxial quasi-substrates: a promising single crystal material for electrochemical sensing applications, Carbon 201 (2022), https://doi.org/10.1016/j.carbon.2022.10.023 published on-line.

[60] R. Trouillon, Y. Einaga, M.A.M. Gijs, Cathodic pretreatment improves the resistance of boron-doped diamond electrodes to dopamine fouling, Electrochem. Commun. 47 (2014) 92–95, https://doi.org/10.1016/j.elecom.2014.07.028.

[61] S. Wang, V.M. Swope, J.E. Butler, T. Feygelson, G.M. Swain, The structural and electrochemical properties of boron-doped nanocrystalline diamond thin-film electrodes grown from Ar-rich and H2-rich source gases, Diam. Relat. Mater. 18 (2009) 669–677, https://doi.org/10.1016/j.diamond.2008.11.033.

[62] D.B. Gorle, M.A. Kulandainathan, Electrochemical sensing of dopamine at the surface of a dopamine grafted graphene oxide/poly(methylene blue) composite modified electrode, RSC Adv. 6 (2016) 19982–19991, https://doi.org/10.1039/C5RA25541D.

[63] X. Liu, D. Ye, L. Luo, Y. Ding, Y. Wang, Y. Chu, Highly sensitive determination of epinephrine by a MnO2/Nafion modified glassy carbon electrode, J. Electroanal. Chem. 665 (2012) 1–5, https://doi.org/10.1016/j.jelechem.2011.06.030.

[64] Q. Li, C. Batchelor-McAuley, R.G. Compton, Electrooxidative decarboxylation of vanillylmandelic acid: voltammetric differentiation between the structurally related compounds homovanillic acid and vanillylmandelic acid, J. Phys. Chem. B 114 (2010) 9713–9719, https://doi.org/10.1021/jp104137p.

PŘÍLOHA II
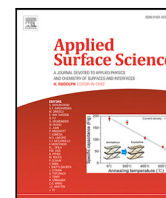
Full length article

Laser-patterned boron-doped diamond electrodes with precise control of sp²/sp³ carbon lateral distribution☆

J. Hrabovsky [a,b,*], M. Zelensky [c], J. Sladek [b,d], M. Zukerstein [b], J. Fischer [c],
K. Schwarzova-Peckova [c], A. Taylor [e], M. Veis [a], S. Mandal [f], O.A. Williams [f], N.M. Bulgakova [b]

[a] Charles University, Faculty of Mathematics and Physics, Prague, Czech Republic
[b] HiLASE Centre, Institute of Physics of the Czech Academy of Sciences, Dolní Břežany, Czech Republic
[c] Charles University, Faculty of Science, Department of Analytical Chemistry, UNESCO Laboratory of Environmental Electrochemistry, Prague, Czech Republic
[d] Faculty of Nuclear Sciences and Physical Engineering, Czech Technical University in Prague, Prague, Czech Republic
[e] FZU – Institute of Physics of the Czech Academy of Sciences, Prague, Czech Republic
[f] School of Physics and Astronomy, Cardiff University, Cardiff, UK

ARTICLE INFO

ABSTRACT

A thorough study on sp³ to sp² carbon conversion in undoped and boron-doped diamond (BDD) thin ($\approx$ 500 nm) layers leading to the desired sp²/sp³ carbon ratio and lateral distribution, which utilizes boron atom incorporation and infrared (IR) material laser processing has been performed. Polycrystalline as-grown (AG) or chem-mechanically polished (CMP) undoped diamond/BDD layers were investigated with respect to boron content and laser wavelength (800, 1030 nm). Boron incorporation leads to an increase in IR optical absorption and reduction of required energy fluence ($F_{th} \approx 1$ J cm^{-2}) needed for sp³ to sp² carbon conversion. Raman spectroscopy was performed to identify carbon conversion stages and to tailor the ideal parameters for other IR laser sources and required sp²/sp³ carbon ratio. Electrochemical parameters (ΔE_p and I_{Ap}/I_{Cp} ratio) were obtained from cyclic voltammetry measurements of outer-($[Ru(NH_3)_6]^{3+/2+}$) and inner-($[Fe(CN)_6]^{3-/4-}$) sphere redox markers. Values of ΔE_p and I_{Ap}/I_{Cp} are mainly influenced after conversion of 10% of sp³ to sp² carbon. This trend is most pronounced for the $[Fe(CN)_6]^{3-/4-}$ redox marker, by decrease or increase of these parameters on AG or CMP BDD electrodes respectively. Electrochemical findings were supported by electrochemical impedance spectroscopy where R_{ct} keeps the same trend as ΔE_p values and double layer capacitance profoundly increases between 10 and 25% of surface conversion.

1. Introduction

Diamond as the hardest among natural materials on earth possesses several unique physical properties such as chemical inertness, biocompatibility or high thermal conductivity while being an insulator material. Boron is one of the most frequently used dopants to generate conductive electrode materials due to its low charge carrier activation energy of ~0.37 eV. Boron doped diamond (BDD) electrodes are widely used in electroanalysis thanks to their electrochemical properties such as a wide potential window in aqueous solutions ($\sim$ 3V), which is caused by high overpotential for the hydrogen and oxygen-generating reactions [1–3]. Other important advantages of BDD electrodes are their exceptional resistance to (bio)fouling and the low capacitance of the BDD layers, which leads to a stable and low background current [1, 3–6].

The electrochemical, physical and optical properties of the BDD electrodes depend on many factors such as dopant concentration, sp² carbon content, surface termination or crystallographic orientation [1–3,7–10]. Surface termination can significantly affect not only the electrochemical properties of the BDD electrodes but also hydrophilicity or hydrophobicity. The surface of BDD electrodes is usually hydrogen-terminated following fabrication by chemical vapor deposition (CVD), which is carried out in a hydrogen-rich atmosphere. The H-terminated electrodes exhibit hydrophobic properties, higher heterogeneous electron transfer kinetics (HET) and better conductivity than O-terminated BDD electrodes. O-terminated BDD electrodes show slower HET kinetics for inner-sphere redox probes and many organic compounds due to the presence of the oxygen functional groups (–COOH, –C–OH, >C=O) possessing π-electrons interacting with the ligand sphere [10,11]. Another important issue is the surface roughness

---

and residual sp^2 carbon content. Regeneration of BDD surface relies on the application of high positive current densities/positive potentials in the region of water decomposition leading to the generation of HO· radicals oxidizing the surface (thus converting it to O-terminated) and adsorbed species [1–3]. Similar, to other carbon-based electrodes, regeneration by polishing with alumina-based or diamond abrasives removes adsorbed species, but also presumably leads to the removal of sp^2 carbon with attached oxygenous functionalities such as –COOH. Polished surfaces possess similar physical and electrochemical properties as H-terminated BDD surfaces [12–14] without affecting the surface topography. Surface roughness can be effectively reduced using chemical mechanical polishing (CMP) for both types, ultra-thin polycrystalline and single crystalline BDD electrodes [15–17]. Previously, we have shown that CMP BDD electrodes possess faster HET kinetics in comparison with as-grown polycrystalline BDD and thus represent an attractive material for sensor designing [17]. Differences are most pronounced for low-doped films. The presence of boron atoms in layers influences the conductivity, therefore BDD electrodes act as semiconductor dielectrics for low boron concentrations ($[B] \leq 3 \times 10^{20}$ atoms cm^{-3}), whereas at higher concentration, above the mentioned limit, exhibit predominantly metallic-like conductivity [8,18,19]. During CVD growth, the process of boron incorporation is accompanied by sp^2 carbon content inclusion in polycrystalline BDD electrodes. In general, sp^2 carbon "impurities" in BDD electrodes lead to the narrowing of the potential window and an increase in capacitive current, which may enhance HET kinetics and significantly affect adsorption processes [9,20]. Since 2007 [21], a limited, but continuous effort to understand the contribution of sp^3 and sp^2 carbon in BDD layers on their electrical, electrochemical, and adsorption properties has been carried out. Undoubtedly, sp^2 carbon may represent the active sites for adsorption and mediate oxidation processes with species formed at sp^3 carbon (*e.g.*, HO·, ClO_3·) [22,23], which is advantageous for the electrocatalytic production of strong oxidants including ozone [20,24]. Other reports presenting the advantages of intentionally fabricated hybrid sp^2/sp^3 carbon electrodes focused on their applications in oxygen and pH sensing [25–27], limited reports exist on detection of inorganic ions [20,28] and simple organic compounds including neurotransmitters [29–31]. In general, it is very difficult to control, spatially and quantitatively, sp^2 carbon content at grain boundaries during CVD. This can be overcome by employing surface/volume laser treatment which can convert sp^3 to sp^2 carbon in selected locations. Creation of spots with sp^2 carbon can be achieved, however some limitations exist due to the laser type and optics used, such as irradiation spot size limit (depends on the laser source and optics used), maximum applied laser fluence of the system, *etc.* [28]. Previous works [25,26] were focused on irradiation of undoped diamond at photon energies below the band gap energy or BDD irradiation at laser wavelengths in the range of 300–550 nm where absorption caused by boron dopants is negligible. This required high laser fluences or repetitive laser treatment of samples, which can cause significant damage to electrodes or induce the creation of defects. Irradiation of thick layers of heavily doped BDD (metallic-like samples) at 800 nm led to the creation of laser-induced periodic surface structures (LIPSS), possessing high double layer capacitance and charge storage capacity. This might be advantageous for the fabrication of cell stimulation electrodes and energy storage such as supercapacitors [32].

Obviously, hybrid sp^2/sp^3 carbon electrodes may benefit from the synergic effect of increased charge storage, charged transfer kinetics and adsorption of inorganic reactive species or organic molecules on sp^2 carbon phase, while keeping the physical and electrochemical properties (*e.g.*, mechanical stability, low background current, wide potential window of the diamond phase). In a wider perspective, they may enable the fabrication of electrochemical (bio)sensors with enhanced sensitivity or selectivity thanks to targeted adsorption of certain compounds (*e.g.*, enzymes, nucleic acids), or in electrocatalytic activity for advanced oxidation processes [28,33]. For these purposes, techniques
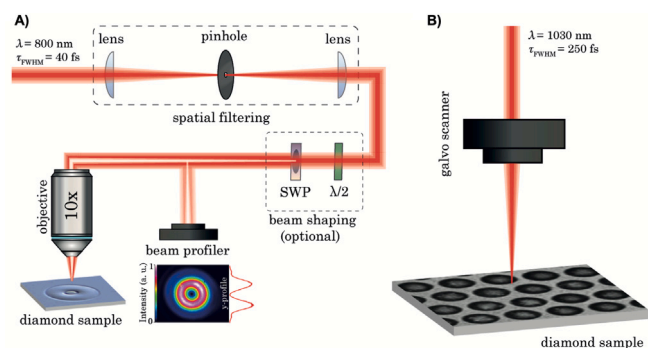

Fig. 1. Simplified experimental scheme of laser processing with (A) Gaussian and doughnut-shaped laser beam (Astrella, 800 nm) and (B) uniform arrays using a galvo scanner with a Gaussian beam (PHAROS, 1030 nm).

Table 1
Values of single pulse threshold fluence F_{th}, beam waist radius w_0 and extinction coefficient k for the two used wavelengths, 1030 nm and 800 nm, obtained for BDD samples with different concentrations of boron.

BDD B/C (ppm)	[B] 10^{21} cm^{-3}	$F_{th,1030}$ J cm^{-2}	$w_{0,1030}$ µm	$F_{th,800}$ J cm^{-2}	$w_{0,800}$ µm	k_{1030}	k_{800}	r_{spot} µm
AG 0	–	1.37	9.13	–	–	0	0	8.7
AG 500	0.66	0.77	9.69	–	–	0.107	0.062	12.5
CMP 500	0.58	0.95	9.73	1.10	2.83	0.107	0.062	11.9
CMP 1000	1.36	0.74	9.62	1.05	2.78	0.398	0.232	14.3
CMP 2000	1.95	0.52	9.59	0.78	2.61	0.689	0.439	17.3

are required to allow surface tuning with controlled distribution of sp^2/sp^3 carbon possessing fit-for-purpose properties.

In this work, a methodology has been developed to precisely pattern surface of thin ($\leq$ 500 nm) as-grown (AG) and chemically mechanically polished (CMP) BDD electrodes with sp^2 carbon by IR femtosecond lasers (800 and 1030 nm) for samples with different boron content. Laser-induced sp^3 to sp^2 carbon conversion was performed in isolated spots which cover the surface area from 0% to 100% of the surface area. The morphology of created Gaussian/doughnut-shaped surface structures (spots) using the highly deterministic femtosecond laser processing was investigated and discussed based on the observations obtained with Raman spectroscopy and spectroscopic ellipsometry. Electrochemical properties were studied using cyclic voltammetry (CV) of outer- and inner-sphere redox markers and electrochemical impedance spectroscopy (EIS) to obtain a complex overview of the influence of sp^2 carbon on the electrochemical performance of the fabricated hybrid sp^2/sp^3 carbon electrodes.

2. Experimental

2.1. Synthesis of polycrystalline BDD layers

Polycrystalline BDD and intrinsic undoped layers were deposited on 2-inch conductive Si wafers using a 1.5 kW resonance cavity microwave plasma-enhanced CVD system (AX5010 from Seki Diamond Systems) using well-established growth conditions similar to Refs. [17, 18]. Thickness of the layers were below $\leq$ 500 nm. Boron doping was obtained by the addition of trimethylboron in the gas phase to provide a B/C ratio ranging from 500 to 2000 ppm (Table 1). The set of the studied samples consisted of "as-grown" electrodes deposited at B/C ratios of 0 ppm and 500 ppm, and chem-mechanically polished electrodes deposited at B/C ratios of 500 ppm, 1000 ppm and 2000 ppm. Electrodes were prepared by the procedure described in our previous study [17] and in more detail in Ref. [15], until RMS roughness was reduced to $\leq$ 2 nm. The prepared electrodes are denoted as AG 0, AG 500, and CMP 500, CMP 1000 and CMP 2000 throughout the text. Following CMP, samples were dipped in HF (54%) to remove

any residual colloidal silica polishing slurry. Both types of BDD-coated wafers were then cut into suitable sizes (5×5 mm^2 and 10×10 mm^2) for further investigations. After laser exposure and completion of all characterization (spectral and electrochemical) measurements, selected samples were exposed to a hot $H_2SO_4 + KNO_3$ mixture to study the stability of the sp^2 carbon phase on the surface *via* Raman spectroscopy.

2.2. Laser surface modification

Laser irradiation and surface treatment were performed by a PHAROS laser system (Light Conversion, $\lambda = 1030$ nm, $\tau_{FWHM} = 260$ fs) and an Astrella laser system (Coherent, $\lambda = 800$ nm, $\tau_{FWHM} \approx 40$ fs). A general scheme of experimental setup is shown in Fig. 1A. Gaussian pulses from the PHAROS laser were focused on the sample surface at normal incidence by a plano-concave lens with focal distance $f = 15$ cm to obtain the dependence of damaged/modified area as a function of applied pulse energy E_{pulse}. Raster scans on BDD surfaces were performed using a Galvo scanner ($f = 16.3$ cm) at a wavelength of 1030 nm with samples placed in a focal position (see Fig. 1B). The peak fluence was the same for all scanned samples with different densities of irradiation spots per unit area. The beam from the Astrella laser (Gaussian-shaped pulses) was spatially filtered by a pinhole (150 μm diameter) in combination with a pair of lenses ($f = 50$ cm) and focused on the sample surface using a microscope objective (10×, NA = 0.12). Doughnut-shaped pulses were generated from the initial Gaussian pulses using an S-waveplate with a half-waveplate to control the (azimuthal/radial) polarization state of the pulses (see Fig. 1A).

2.3. Characterization methods

Structural and chemical analysis was carried out by Raman spectroscopy at room temperature using a Renishaw InVia Raman Microscope at 488 nm (laser power of 6 mW). Spot characterization was realized using a 50x objective. For the determination of boron concentration [B] method I in the range from 1100 to 1500 cm^{-1} described in detail in Ref. [18] was used. Values for the sp^2/sp^3 carbon ratios were obtained by fitting the Raman spectra, over the 1000 – 1700 cm^{-1} range, to derive curve/peak integrated area values using Renishaw WiRE 3.2 software. Values were then used, according to [34], to determine a layer quality factor f_q indicating the sp^2/sp^3 carbon ratio (see Table S1). Values of the extinction coefficient used in this article were taken from the experimental data obtained by spectroscopic ellipsometry (SE) using the general Model I described in Ref. [18] as the reported samples were prepared using the same conditions. Laser-structured/modified surfaces were inspected using a confocal laser-scanning microscope (Olympus OLS5000). The determination of the laser-induced damage threshold was based on measurements of the damaged spot area S, as a function of the applied laser pulse energy E_0, using the D^2 method [35,36]. This method is based on the following relationship between S and E_0 for Gaussian beams:

$$S/S_{eff} = \frac{\ln(E_0/E_{th})}{2} \qquad (1)$$

where $S_{eff} = \pi w_0^2$ is the cross-sectional area of the beam focused on the surface with w_0 being the beam waist radius (the $1/e^2$ criterion) and E_{th} is a pulse threshold energy, *i.e.* minimal energy needed to produce visible modification on the sample surface. Consequently, the effective spot area and the threshold energy can be extracted from the least square fit of a linear dependency $S(\ln(E))$. The peak threshold fluence F_{th} can be calculated as $F_{th} = 2E_{th}/S_{eff}$. Note, the F_{th} value should be the same for Gaussian and doughnut-shaped pulses [37].

Electrochemical analysis was performed using hexaammineruthenium(II) chloride (Sigma-Aldrich, Germany), potassium hexacyanoferrate(III), and potassium chloride (Lach-Ner, Neratovice, Czech Republic). All chemicals were of analytical grade and were used without any further purification. Deionized water (Millipore Mili plus Q system,

Billerica, USA) with a resistivity of not less than 18.2 MΩ cm was used to prepare all aqueous solutions. For CV measurements, a three-electrode setup was used, consisting of an Ag/AgCl/3 mol L^{-1} KCl reference electrode and a platinum wire as an auxiliary electrode (both from Elektrochemicke detektory, Turnov, Czech Republic). Working BDD electrodes were constructed by placing the sample in a Teflon electrode body with rubber sealing. The exposed geometrical area of the electrode was $S_{geom} = 3.5$ mm^2. CV measurements were performed using a Palm-Sens potentiostat with PSTrace 5.8 software (PalmSens BV, Houten, The Netherlands).

The apparent heterogeneous electron transfer rate constant k^0_{app} values were calculated from the peak potential difference of anodic and cathodic peak ΔE_p estimated from CVs of 1 mmol L^{-1} [Fe(CN)$_6$]$^{3-/4-}$ and [Ru(NH$_3$)$_6$]$^{3+/2+}$ recorded at the scan rate of 100 mV s^{-1} [38]. The diffusion coefficients of 7.6×10^{-6} cm^2 s^{-1} for [Fe(CN)$_6$]$^{3-/4-}$ [39] and 5.5×10^{-6} cm^2 s^{-1} for [Ru(NH$_3$)$_6$]$^{3+/2+}$ [40] were used for the calculation. The rate constants are referred to as apparent ones, because no correction for electric double-layer effects was made.

EIS measurements were carried out using an Autolab PGSTAT101 potentiostat with Nova 2.1 software (Metrohm Autolab B.V., Utrecht, The Netherlands). Impedance spectra in 1 mol L^{-1} KCl in the presence of 1 mmol L^{-1} [Fe(CN)$_6$]$^{3-/4-}$ were measured at a potential of $E = +0.3$ V. Amplitude of measurements was 10 mV over a frequency range from 100 kHz to 1 Hz. Data were fitted by equivalent circuits (depicted in Fig. S4) containing an ohmic resistance (R_{ohm}), constant phase element (CPE) and charge transfer resistance (R_{CT}), and Warburg impedance (W) in the case Nyquist plots showed a significant part of mass transfer control. Consequently, R_{CT} and Y_0 parameters were evaluated. To normalize capacitance Y_0, modified surface areas S_{real} were calculated from atomic force microscopy (AFM) measurements used in our previous study [17] (the post-irradiation real surface area increase was negligible as confirmed by confocal microscopy). For AG 0 electrodes, the same surface area difference as for AG 500 electrodes was used as their surface roughness was similar. In calculations, S_{real} values of 0.0356 cm^2 and 0.0350 cm^2 were used for AG and CMP BDD electrodes respectively.

3. Results and discussion

3.1. Modification threshold and surface morphology

In the case of transparent materials or materials with low extinction coefficients, ultrashort femtosecond laser pulses play a key role in material processing due to the increased efficiency of non-linear photoionization. For small band-gap materials, linear and nonlinear (multiphoton/tunnelling) photoionization is efficient enough to reach critical electron density which results in observable irreversible structural changes. For large band-gap materials, it is known that photoionization is the mechanism that creates seed electrons, which, upon absorbing laser light via inverse bremsstrahlung, initiate impact (avalanche) ionization. The latter significantly contributes to free electrons generation which results in optical breakdown. Diamond with indirect ($E_g^{in} = 5.49$ eV [41]) and direct ($E_g^{dir} = 7.3$ eV [41]) bandgap energies lies in an intermediate zone between materials with relatively small bandgap energy ($E_g \leq 4.4$ eV) and large-bandgap dielectrics such as fused silica ($E_g \approx 9$ eV) or YAG ($E_g \approx 8$ eV [42,43]) and LuAG ($E_g \approx 8.2$ eV [44]) crystals. In [18] we showed that the optical bandgap energy of CVD single crystal diamond fabricated in our lab was verified, using spectroscopic ellipsometry, as $E_g = 5.58$ eV, therefore we can consider that both nonlinear photoionization and avalanche ionization take place during material processing with ultrashort laser pulses.

For easier interaction of the incident radiation with diamond and therefore a higher absorption rate, CVD grown diamond can be doped with boron atoms. Boron doping results in an increase in absorption in the infrared (IR) part of electromagnetic spectra due to the creation of free carriers (holes) in the material [18,45]. The results summarized in
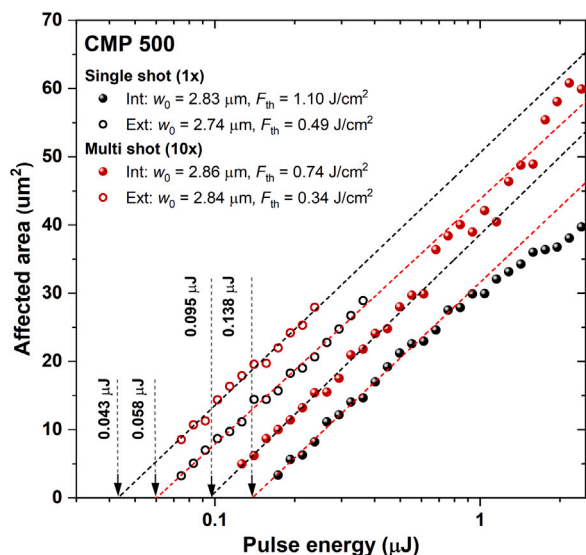
Fig. 2. Areas of damaged spots produced on CMP 500 surface with femtosecond (Astrela: 40 fs, 800 nm) pulses as a function of laser pulse energy. Lines represent the least-square fits according to Eq. (1). Measured threshold energies, effective spot radii w_0, and threshold fluences (F_{th}) are indicated for the double-ring structure (see images in Fig. 3).

Table 1 showed that in this case the optical absorption then naturally increases with increasing wavelength of light. This and favours laser processing of BDD with radiation sources operating in the infrared region of the spectrum, although at photon energies smaller than the bandgap energy. This is a significant advantage compared to previous works where 355 nm [26] and 532 nm [25] nanosecond laser sources were used. These energies are also located in the wavelength range below the optical bandgap energy of the undoped diamond but they cannot be efficiently absorbed by free carriers to initiate the avalanche process in BDD.

Initial Raman investigation confirmed boron incorporation into the polycrystalline BDD layers from $\approx 0.6 \times 10^{21}$ cm^{-3} (AG 500 and CMP 500) to $\approx 2.0 \times 10^{21}$ cm^{-3} (CMP 2000) (Table 1); $i.e.$, above the theoretical threshold of semi metallic/metallic type of conductivity of 0.2×10^{21} cm^{-3} [19]. Further, all layers were sp^3 carbon-rich in composition, characterized by f_q ranging from 0.95 (CMP 2000) to 0.97 (AG 0) (Supplementary Information, Table S1). To verify the influence of boron doping and/or surface defects in the BDD layers on laser material processing, damage threshold measurements were performed over a wide range of laser fluences and two regimes (single- and multi-pulse irradiation) using two femtosecond laser sources operating at 800 nm (40 fs, Gaussian/doughnut-shaped pulses) and 1030 nm (250 fs, Gaussian pulses). Firstly, BDD samples were irradiated with 800 nm Gaussian pulses. The obtained dependencies of the affected area as a function of the pulse energy are shown in Fig. 2 for single and multiple (10×) pulse irradiation for sample CMP 500. Using optical microscopy, a zone consisting of double-ring structure is observed for most irradiation regimes, with an internal (Int) strongly modified dark area and (Ext) a lighter surrounding ring (Fig. 3). Their radii (w_0) and corresponding fluences (F_{th}) are given in Fig. 2. The origin of this double-ring structure is discussed further below.

Irradiated spots were studied using Raman spectroscopy and both confocal and conventional optical microscopy techniques, which enabled detection of not only visual and morphological but also phase changes on the surface. Raman spectrum of pristine, non-irradiated BDD is shown in Fig. 3A (with associated images from optical and confocal microscopy) with characteristic diamond (1324 cm^{-1}) and boron-originated (1250 cm^{-1}) bands. The observed feature at ≈ 1530 cm^{-1} is usually matched with the presence of transpolyacetylene (TPA) or

amorphous carbon [18]. A broad band between approximately 935 and 990 cm^{-1} is associated with silicon, from the underlying substrate, and is also detectable for non-irradiated samples due to their low thickness and a partial transmission (BDD samples with B/C $\leq$ 1000 ppm) of the laser wavelength used.

From irradiated spots images and their corresponding Raman spectra (Fig. 3), it follows that laser pulses penetrate and ablate the BDD layer at sufficiently large fluences and produce almost rimless shallow craters (Fig. 3D–E). With respect to the used laser fluences, the resulting craters may contain a residual amount sp^2 carbon formed by laser-induced conversion, shown in Raman spectroscopy by two characteristic D (1352 cm^{-1}) and G (1588 cm^{-1}) bands together with a background Si band (Fig. 3 spectra D), or solely the broad Si band at maximal laser fluences used (Fig. 3 spectra E). With decreasing laser fluence, the pulse energy is not high enough to remove/redeposit the BDD layer material. Instead, it causes the protrusion of the modified material above the initial surface which consists predominantly consisting of the sp^2 carbon (Fig. 3C and C*). The observed protruded structure becomes smaller with decreasing pulse energy until its complete disappearance for energy corresponding to E_{th}(Fig. 3B). With decreasing laser fluence toward E_{th}, the thickness and the radius of the sp^2 carbon laser-created zone gradually decreases. Correspondingly, Raman spectra show a gradual increased presence of silicon and boron bands reaching a maximum at the point where the response is similar to non-irradiated BDD when the pulse energies of $E < E_{th}$. Analogous behaviour has been observed using multiple pulse irradiation (Fig. 2) followed by a decrease in threshold fluence from $F_{th,800}^S = 1.1$ J cm^{-2} (single pulse) to $F_{th,800}^M = 0.74$ J cm^{-2} (10 pulses) and, moreover, narrowing of the energy range for which only sp^2 carbon was detected.

Additionally, doughnut-shaped laser pulses were used for irradiation of BDD samples to demonstrate the flexibility of IR lasers to convert carbon hybridization from sp^3 to sp^2 in selected areas of the surface. Results are presented in Fig. 3 for both (C*) single pulse and (E) multi-pulse irradiation. The main advantage of using doughnut-shaped pulses is preservation of the central part of the laser spot which contains pristine sp^3 carbon. The chemical and structural composition of the surrounding ring is then dependent on the laser fluence (as described above) and can be selectively chosen. This shape flexibility of the surface containing sp^3 or sp^2 carbon might be advantageous for tailoring surface adhesion properties for functionalization by attachment of organic molecules or biopolymers (enzymes, nucleic acids) for the construction of (bio)sensors.

Further, we have investigated the possibility of BDD surface structuring by selective removal of laser-created sp^2 carbon phase. Exposure of the surface to a hot mixture of H$_2$SO$_4$ + KNO$_3$ for 15 min resulted in the removal of non-diamond carbon from the surface structure. The surface itself remains morphologically altered but does not exhibit any sp^2 carbon Raman signal as can be seen in Fig. 3 (dashed lines). The depth and the lateral size of the remaining craters are then proportional to the applied pulse energy. Thus, the combination of laser treatment and acid washing enables a diamond surface structuring prospective for fabrication of electrodes with an enlarged area with desired patterns applicable in (bio)sensing or advanced oxidation processes benefiting from increased production of reactive species. Moreover, the main advantage of this acid-cleaning method is that BDD electrodes can be easily reactivated and reused. However, the surface characteristics of acid-treated laser irradiated spots require further investigation to confirm, for example, the presence, or not, of a stable "mono-layer" sp^2 carbon phase, which is insensitive to Raman spectroscopy.

An additional effect to highlight is the appearance of a second (external) ring around the original protruded spot following laser treatment. Both, the internal and external zone are graphically marked in Fig. 4 for AS 500 sample. The presented effect has even been observed for pulse energies well below the obtained damage thresholds of BDD samples. Interestingly, this effect does not cause any significant changes in the morphology and the structure of the BDD layer as
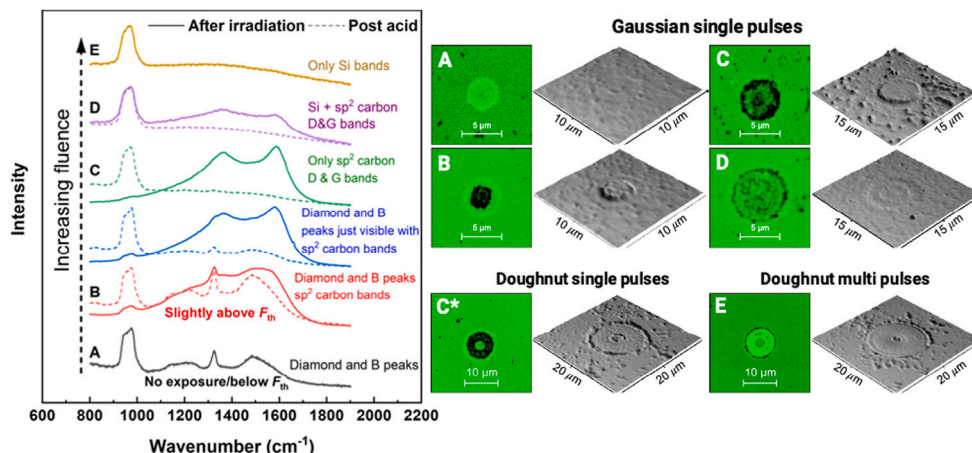
Fig. 3. Model examples of obtained Raman spectra for five characteristics regimes with respect to increasing laser fluence (left) and the corresponding optical and confocal images of the created sp^2 carbon spots on CMP 500 sample. The Raman spectra are presented for the samples directly after irradiation (solid lines) and after acid cleaning (dashed lines).
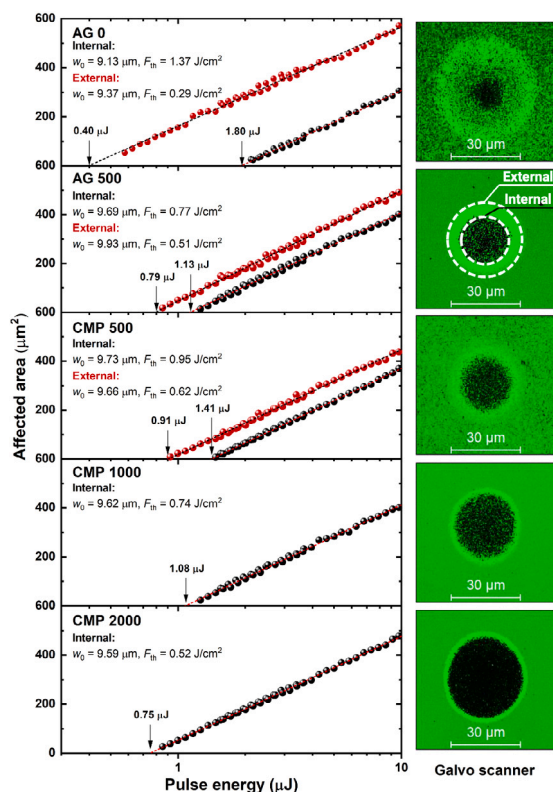

Fig. 4. Areas of the damaged spots produced on AG and CMP diamond surfaces with different boron content with femtosecond (PHAROS: 250 fs, 1030 nm) laser pulses as a function of pulse energy. Lines represent least-square fits according to Eq. (1). Measured threshold energies, effective spot radii (w_0), and threshold fluences (F_{th}) are indicated. Confocal images on the right represent the laser-modified spots on the studied AG and CMP diamond surfaces using a Galvo scanner at the same laser fluence, $F = 4$ J cm^{-2}.
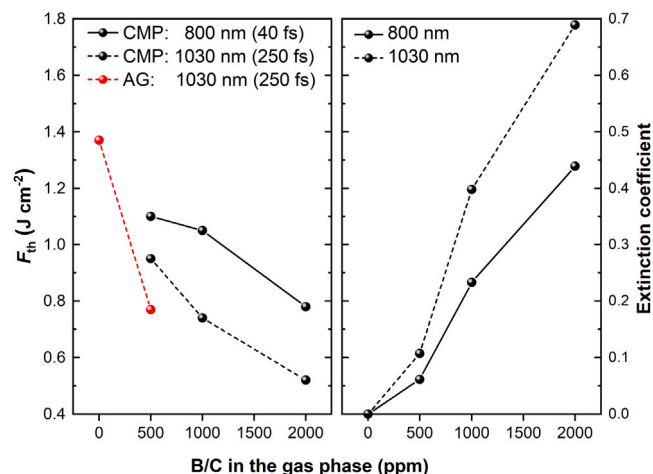

Fig. 5. The threshold fluences F_{th} (left) for CMP and AG samples and the corresponding extinction coefficients (right) for two used wavelengths, 800 and 1030 nm.

can be seen in Fig. 3A. A similar double structure was observed for both wavelengths 800 and 1030 nm wavelengths (see Figs. 2 and 4). The corresponding plots of the dependence of the external ring area on the applied pulse energy exhibit practically the same experimental parameter of the beam waist as compared to that obtained from fitting the internal pattern characterized by material protrusion. On the example of Astrela laser (800 nm), it is also visible for both single pulse ($w_{0,Int}^S = 2.83$ µm, $w_{0,Ext}^S = 2.74$ µm) and for multiple

pulse ($w_{0,Int}^M = 2.84$ µm, $w_{0,Ext}^M = 2.86$ µm) irradiation regime. Damage thresholds were then estimated as $F_{th,800} = 0.49$ J cm^{-2} for the single pulse and $F_{th,800} = 0.34$ J cm^{-2} for 10-pulses irradiation. Note, diamond is a transparent material at 800 nm, and BDD samples with a low boron content exhibit low values of extinction coefficient (see Table 1) as was observed in our previous study [18]. Using the known value of the extinction coefficient, we can calculate the exact value of the penetration depth as a function of boron content, which is certainly larger than the sample thickness for materials with B/C ≤ 500 ppm (Figure S1). Thus, combining the previous findings, it can be confidently concluded that the external modification ring can be assigned to structural modification of the silicon substrate as the available literature data at $\lambda = 800$ nm refer to the silicon threshold values of annealing ($F_{ann} = 0.55$ J cm^{-2}) and modification ($F_{mod} = 0.26$ J cm^{-2}) [46]. A similar observation has been made for $\lambda = 1030$ nm (see Fig. 4), where results were compared with the corresponding threshold fluences of modification ($F_{mod} = 0.226$ J cm^{-2}) and melting ($F_{mod} = 0.408$ J cm^{-2}) of silicon obtained using a similar laser source [47,48].

Boron incorporation into the BDD layers considerably increases the optical absorption as illustrated in Fig. 5. For samples grown with B/C ≥1000 ppm, the incident light is completely absorbed within the BDD layer (penetration depth is smaller than the layer thickness, see
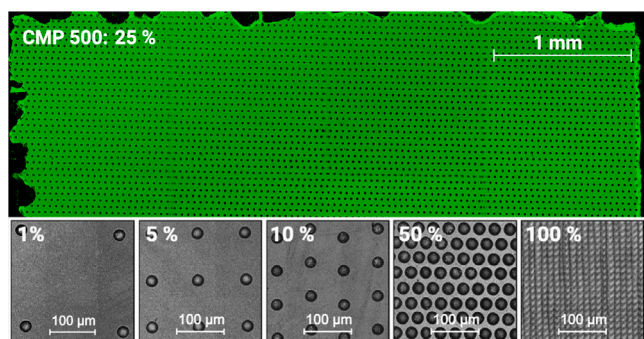
Fig. 6. Confocal images of the laser-modified spot arrays on CMP 500 produced by irradiation with single shot per spot (1030 nm, Gaussian pulses) at a laser fluence of 4 J cm^{-2} for the increasing sp^2 carbon area fractions of 1, 5, 10, 50 and 100%.

Figure S1). Thus, there is no significant change in the silicon substrate as was observed previously for the low-doped boron samples. This enhanced absorbance causes a decrease in threshold fluence F_{th} as a function of boron concentration for both used wavelengths. Also, threshold fluence decreases with increasing light wavelength for a constant boron concentration (Table 1). Irradiated BDD layers were further analysed with respect to the initial surface quality (CMP vs. AG). A slight decrease was observed in the threshold fluence for the AG compared to CMP samples, which was attributed to the higher surface roughness and/or a higher concentration of surface defects due to the polycrystalline character of AG samples. The derived parameters of the threshold fluences and the beam waist radii for both 800 nm (Fig. 2) and 1030 nm (Fig. 4) are given in Table 1.

Obtained results allow improved tailoring of the sp^2/sp^3 carbon ratio on the BDD surface at relatively low laser fluences. Compared to previous studies [25,26] this is enabled by boron incorporation allowing an increase in laser energy absorption and thus a reduction in the required energy needed for surface processing. Fig. 4 shows the difference between modified spots produced by a Galvo scanner ($f = 16.3$ cm, $w_0 = 13.5$ μm) at a constant laser fluence of 4 J cm^{-2} (1030 nm, 250 fs), which was for undoped diamond (AG 0) barely sufficient to observe sp^2 carbon formation on the surface but was sufficient enough to produce relatively large areas of sp^2 carbon on BDD samples with measurable boron concentrations.

Using these conditions, a set of electrodes with different concentrations of boron for electrochemical analysis were prepared using a synchronized Galvo scanner with different ratios of sp^3 to sp^2 carbon converted surfaces: 0.0, 0.1, 1.0, 5.0, 10, 25, 50 and 100%. This percentage factor was defined as the ratio between the sum of derived spot areas of radius $w_0 = 13.5$ μm (Galvo scanner) per unit electrode area and was varied by changing the centre-to-centre distances between the adjacent irradiation spots from ~763 μm (0.1% surface conversion) to ~14 μm (100%). Illustrative sections from confocal images of the fabricated CMP 500 electrodes (5 × 5 mm^2) with various sp^2 carbon area friction are shown in Fig. 6.

3.2. Electrochemical characterization of BDD electrodes

The electrochemical characterization of laser-irradiated BDD electrodes with the different percentages of the converted surface from sp^3 to sp^2 carbon (0, 0.1, 1, 5, 10, 25, 50 and 100%) was performed to confirm the presence and stability of the sp^2 carbon sites on the surface, to identify the limits of alteration of the electrochemical properties from pure sp^3 carbon electrodes to hybrid sp^2/sp^3 carbon and finally to completely sp^2 carbon electrodes. For this purpose, the difference of potentials of the anodic and cathodic peaks (ΔE_p) and the ratio of anodic to cathodic peak currents (I_{Ap}/I_{Cp}) reflecting HET kinetics of redox reactions were evaluated from CV measurements of 1 mmol L^{-1} inner-
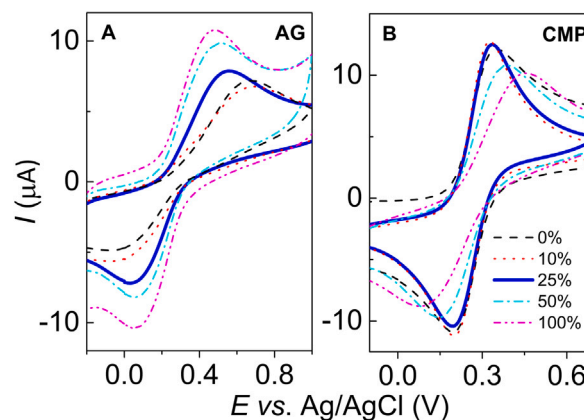

Fig. 7. Cyclic voltammograms of 1 mmol L^{-1} [Fe(CN)$_6$]$^{3-/4-}$ for (A) AG 500 and (B) CMP 500 electrodes with sp^2 carbon area fraction: 0% (black, – –), 10% (red, ··), 25% (blue —), 50% (cyan, –·–), and 100% (magenta,–··–). Supporting electrolyte 1 mol L^{-1} KCl, scan rate 0.1 V s^{-1}.

Table 2
Values of peak potential difference of anodic and cathodic peak ΔE_p estimated from CVs of 1 mmol L^{-1} [Fe(CN)$_6$]$^{3-/4-}$ and [Ru(NH$_6$)$_6$]$^{3+/2+}$ recorded on all AG and CMP BDD electrodes with laser-induced sp^3 to sp^2 carbon (sp^2/sp^3-C) conversion ranging from 0% to 100% (first column) of the surface area. CV: supporting electrolyte 1 mol L^{-1} KCl, scan rate 0.1 V s^{-1}.

	[Fe(CN)$_6$]$^{3-/4-}$					[Ru(NH3)$_6$]$^{3+/2+}$				
	ΔE_p (mV)					ΔE_p (mV)				
sp^2/sp^3-C (%)	AG 0	AG 500	CMP 500	CMP 1000	CMP 2000	AG 0	AG 500	CMP 500	CMP 1000	CMP 2000
0.0%	–	429	120	93	81	165	72	60	60	60
0.1%	–	315	114	93	75	240	84	66	60	60
1.0%	–	375	–[a]	90	81	201	63	60	60	57
5.0%	–	261	117	93	84	186	66	60	57	57
10%	–	585	135	96	90	144	69	60	60	63
25%	723	477	129	120	120	99	66	60	60	57
50%	447	393	195	105	408	72	60	60	57	57
100%	297	423	321	258	405	60	60	60	60	57

[a] Electrodes were broken during measurements.

([Fe(CN)$_6$]$^{3-/4-}$) and outer-sphere ([Ru(NH$_3$)$_6$]$^{3+/2+}$) redox markers in 1 mol L^{-1} KCl. The potential window used during the CV was chosen to avoid water electrolysis reactions leading to hydrogen/HO· radical formation at the negative/positive potential limit. Thus, prevention of surface oxidation/reduction was assured as well as protection of sp^2 carbon spots which could be damaged by HO· radicals formed on the BDD surface [32,49,50]. For a broader investigation, the charge transfer resistance (R_{ct}) and the capacitance values (Y_0) were obtained by EIS in 1 mol L^{-1} KCl in the presence of 1 mmol L^{-1} [Fe(CN)$_6$]$^{3-/4-}$.

Obtained ΔE_p values for [Fe(CN)$_6$]$^{3-/4-}$ and [Ru(NH$_3$)$_6$]$^{3+/2+}$ are summarized for all electrodes in Table 2, their recalculation by the Nicholson method [38] to apparent heterogeneous electron transfer rate constant k^0_{app} values is reported in Table S2 for all tested inorganic redox markers and Table S3 reports on I_{Ap}/I_{Cp} values. Illustrative CVs for [Fe(CN)$_6$]$^{3-/4-}$ are for CMP and AG 500 electrodes depicted in Fig. 7. The CVs recorded on other BDD electrodes are depicted in Supplementary information (Figure S2 for [Fe(CN)$_6$]$^{3-/4-}$, Figure S3 for [Ru(NH$_3$)$_6$]$^{3+/2+}$). In general, for sp^2 carbon area fraction from 0% to 25% ΔE_p values and I_{Ap}/I_{Cp} ratio did not hold any visible trend. Thus, 25% of sp^2 carbon area presented a threshold; a higher area percentage of sp^2 carbon influenced significantly the electrochemical behaviour of the hybrid sp^2/sp^3 carbon electrodes, and, naturally dominated their behaviour for 100% area conversion. This is a surprisingly high value when the effect of sp^2 carbon on the electrochemical properties of diamond electrodes is considered. The key role in their alteration play oxygen functionalities [51,52] and increased adsorption

on sp^2 carbon-rich domains, as adsorption of intermediate species favours electrocatalytic processes including hydrogen/oxygen evolution reaction limiting the potential window. Thus, BDD electrodes with higher sp^2/sp^3 carbon ratio possess narrower potential window, higher wetability, and increased double layer capacitance in comparison with BDD electrodes with minimal sp^2 carbon content [9,20,24,33]. However, most of the published studies refer to properties of heterogeneous diamond electrodes with sp^2 carbon present in intentionally fabricated diamond nanostructures [30,53] or at the crystallite grain boundaries, thus being relatively uniformly distributed over the entire surface as result of the film growth at steady conditions during CVD [33,54,55]. Importantly, both boron incorporation and sp^2 carbon formation is directly linked to carbon/hydrogen ratio (with higher B incorporation for higher C/H ratio) and film morphology [33,54–56], which complicates the interpretation of observed electrochemical and electronic characteristics of hybrid sp^2/sp^3 carbon electrodes. Typically, significant changes (increase of background current, narrowing of potential window, changed HET kinetics of redox markers) have been reported even for minimal sp^2 carbon content in comparison with pure BDD electrodes [9,24]. However, quantitation of sp^2 carbon in bulk sp^3 carbon is problematic, thus the studies typically operate with C/H ratio used during deposition (typically altered from 0.5% to 3%). Laser irradiation enables located treatment of diamond surfaces and dramatic increase of double layer capacitance or faster HET kinetics of redox markers have been reported [25,32]. However, in these studies either the entire surface [32] or its substantial fractions (increase of effective surface area by 41.7% reported in [25]) were laser-textured. Our results revealed that sp^2 carbon content does not influence significantly the electrochemical characteristics of studied BDD electrodes up to 25% of area fraction, corresponding to sp^2 carbon spot radius of about 13.5 µm and spot centre-to-centre distance of 46 µm. The reason could be (i) spatial distribution, and (ii) the character of sp^2 carbon formed by laser-induced transformation. Obviously, the electrochemical activity of the hybrid sp^2/sp^3 carbon electrodes was up to this ratio dominated by the activity of the BDD fraction. Thus, BDD presented the material with higher electrochemical activity than the laser-formed sp^2 carbon concentrated in isolated spots and the diffusional overlap developed during redox reactions of markers enabled masking of these sp^2 carbon areas with lower activity.

The effect of sp^2 carbon fraction was well reflected in parameters obtained on the undoped AG 0 electrode. In principle, it should be non-conductive, as Raman shows that boron and sp^2 carbon are not present. However, ΔE_p values of 165 mV for $[Ru(NH_3)_6]^{3+/2+}$ showed that even undoped diamond electrodes with no laser irradiation show enough conductivity to produce a quasi-reversible redox signal for this outer-sphere redox marker. Similar feature was reported for diamond films deposited by hot-filament CVD [55]. This was most likely caused by a trace amount of boron in the CVD reactor which was incorporated into the layer during its growth, *i.e.*, background levels of B in the growth chamber, which is an unavoidable issue for reactors commonly used to produce BDD films. Values of ΔE_p for $[Fe(CN)_6]^{3-/4-}$ on undoped diamond could not be estimated, as the cathodic peak was not developed. However, for both redox markers significant changes in ΔE_p values could be recorded when reaching 25% of area conversion. For $[Ru(NH_3)_6]^{3+/2+}$ the most pronounced drop in ΔE_p values was found between 10% and 25% of sp^2 carbon area fraction (144 mV to 99 mV) with a further decrease to $\Delta E_p = 60$ mV for 100%. This was supported by the I_{Ap}/I_{Cp} ratio, which was improved with increasing sp^2 carbon content from 0.46 (0% of area conversion) to 1.18 (100%). ΔE_p values for $[Fe(CN)_6]^{3-/4-}$ started to decrease rapidly from 723 mV to 297 mV with increasing sp^2 carbon area fraction from 25% to 100%. Simultaneously, I_{Ap}/I_{Cp} ratio changed from 1.89 to 0.95. Obviously, laser-introduced sp^2 carbon increases the conductivity of the original material (*i.e.* undoped diamond) possessing minimal conductivity, facilitates electron transfer, significantly for area fractions > 25%, resulting in quasi-reversible or even reversible character (for ($[Ru(NH_3)_6]^{3+/2+}$)

of the redox reaction. The change in electrochemical behaviour for sp^2 carbon area fractions > 25% is obvious also from the data obtained for AG and CMP BDD electrodes. In our previous study [17] we confirmed more uniform distribution of conductivity and thus faster HET kinetics for CMP in comparison with AG BDD electrodes. These trends were more pronounced for low-doped electrodes (CMP 500–2000 electrodes) [17]. This difference is reflected in ΔE_p values for CMP 500 being lower than for and AG 500, naturally, more significantly for $[Fe(CN)_6]^{3-/4-}$ than for $[Ru(NH_3)_6]^{3+/2+}$ (Table 2).

When comparing ΔE_p values of both redox markers obtained on AG 500 electrode, no clear trend is obvious for $[Ru(NH_3)_6]^{3+/2+}$ with increasing sp^2 carbon fraction. Low values from 84 mV to 66 mV were obtained, common for this marker [12,57]. For $[Fe(CN)_6]^{3-/4-}$, in general, higher values were obtained for sp^2 carbon fraction $\leq$ 10%, reaching values from 393 mV (AG 500 with 50% surface conversion) to 585 mV (AG 500 with 10% surface conversion) confirming decelerated kinetics in the presence of sp^2 carbon and confirming its significant role in the electron transfer process. The variance of the values for sp^2 carbon fraction $\leq$ 5% (261 mV–375 mV) relate to the construction of the electrode with a relatively small geometric surface area exposed to the measured solution. From the whole surface of electrode ($S = 5{\times}5$ mm^2) only $S_{geom} \sim 3.5$ mm^2 was in direct contact with the solution. So, it is highly possible that every time the electrode is mounted to the electrode body, a different number of sp^2 carbon spots were in direct contact with the solution. For instance, the difference in exposed spots on electrodes with 1% surface laser irradiation could vary from 44 to 52 spots (*e.g.*, a variation of about 18%).

For all studied CMP BDD electrodes (500 ppm, 1000 ppm, 2000 ppm) differences in HET kinetics with increasing sp^2 carbon fraction were much more pronounced than for AG BDD electrodes. For $[Fe(CN)_6]^{3-/4-}$, ΔE_p values were rather constant for 0%–10% surface irradiation (ranging from 75 mV (corresponds to $k^0_{app} = 0.017$ cm s^{-1}) to 135 mV ($k^0_{app} = 0.003$ cm s^{-1}), influenced rather by boron than sp^2 carbon content. Relatively low values were obtained (*e.g.*, from 120 mV to 81 mV for CMP 500 to 2000 with 0% or from 135 mV to 90 mV for CMP 500 to 2000 with 10% conversion) confirming accelerating HET kinetics with increasing boron content on smooth CMP surfaces, dominantly governed by the sp^3 carbon fraction. For sp^2 carbon fraction > 25% ΔE_p values increased significantly, reaching values from 321 to 405 mV for CMP BDD 500 to 2000 with 100% conversion. Obviously, HET kinetics were influenced by the sp^2 carbon fraction obtained by laser irradiation. The I_{Ap}/I_{Cp} ratio (Table S3) confirmed this with values around 1 for CMP BDD electrodes with sp^2 carbon conversion less than 25% and, above this sp^2 carbon fraction, threshold values increased to around 1.2, thus indicating significant quasi-reversibility of the system.

For $[Ru(NH_3)_6]^{3+/2+}$ as a surface insensitive probe, low ΔE_p values in the range from 57 mV to 63 mV were obtained irrespective of the boron and sp^2 carbon content for all studied CMP BDD electrodes. The ΔE_p values are reflected in high k^0_{app} values of 0.033–0.164 cm s^{-1} (Table S2), comparable with polycrystalline BDD electrodes [12,17]. The only obvious effect is that the low value of 57 mV was obtained on CMP 1000 and 2000 electrodes, more frequently for those with higher sp^2 carbon fraction. Values lower than 59 mV are closely connected with oxygen functional groups on sp^2 carbon. In this case, the partial negative charge of these groups promotes the adsorption of positively charged $[Ru(NH_3)_6]^{3+/2+}$ [9]. Differences among electrodes with low and high (> 25%) sp^2 carbon area fraction are highlighted in the I_{Ap}/I_{Cp} ratio, increasing from values of about 1 for CMP 0%–10% electrodes to 1.16–1.22 for CMP 100% converted electrodes indicating quasi-reversibility of the redox reaction.

Comparison of ΔE_p values for 100% sp^2 carbon area fraction is useful for characterization of its electrochemical activity. While for $[Ru(NH_3)_6]^{3+/2+}$ values nearing to the theoretical value of 59 mV for reversible redox processes were obtained, for $[Fe(CN)_6]^{3-/4-}$ ΔE_p values ranged from 258 mV (CMP 1000) to 423 mV (AG 500). These values

Table 3

Calculated and fitted Y_0 and R_{ct} parameters from EIS data for BDD electrodes with laser-induced sp^2 to sp^3 carbon (sp^2/sp^3-C) conversion ranging from 0% to 100% (first column) of the surface area. EIS performed in 1 mol L^{-1} KCl in the presence of 1 mmol L^{-1} [Fe(CN)$_6$]$^{3-/4-}$ at a potential of $E = +0.3$ V. Impedance of the CPE was calculated as $Z_Q = 1/Y_0(j\omega)^n$. The units of Y_0 is μmho s^{-1} cm^{-2}.

sp^2/sp^3-C	AG 0		AG 500		CMP 500		CMP 1000		CMP 2000	
(%)	Y_0	R_{ct} (kΩ)	Y_0	R_{ct} (kΩ)	Y_0	R_{ct} (kΩ)	Y_0	R_{ct} (kΩ)	Y_0	R_{ct} (kΩ)
0.0%	13.2	959	11.5	65.5	–[a]	–[a]	–[a]	–[a]	18.6	1.01
0.1%	3.84	744	13.7	33.8	–[a]	–[a]	18.6	1.59	20.6	1.03
1.0%	9.44	621	22.6	24.9	–[a]	–[a]	21.1	1.69	22.4	0.88
5.0%	9.80	710	11.8	19.4	17.3	2.74	22.1	2.28	38.6	1.01
10%	7.67	443	30.9	57.5	22.7	3.8	35.4	2	56.0	1.18
25%	13.0	253	53.1	23.4	37.4	5.14	57.1	4.13	–[a]	–[a]
50%	56.2	20.1	114	19.5	79.4	20	121	9.35	216	28
100%	188	42.4	348	32.7	238	17.6	193	10	286	19

[a] Electrodes were broken during measurements.

reveal decelerated HET kinetics, ascribed on carbonaceous electrodes to interaction of ligand sphere with π electron systems present in carbon-attached oxygen functionalities [11] or lower conductivity of the material itself. Active carbon electrodes exhibiting fast HET kinetics as polished glassy carbon (GC) [58] or edge plane pyrolytic graphite (PG) [59] possess in general lower ΔE_p values. Higher values of ΔE_p were obtained *e.g.*, on basal plane PG [60]. The herein reported values are usual for common carbon paste electrodes [61], some types of GC [62,63] or freshly cleaved basal plane PG [60], where the electron transfer is influenced by heterogeneity of the material or decreased conductivity into the bulk of the material (for basal plane PG).

Further, EIS measurements were carried out to describe the influence of sp^2 carbon on charge transfer resistance R_{ct} and the parameter Y_0 describing the capacitance of the double layer of all studied AG and CMP BDD electrodes. Parameters are listed in Table 3 and were evaluated from Nyquist plots of 1 mmol L^{-1} [Fe(CN)$_6$]$^{3-/4-}$ in 1 mol L^{-1} KCl at $E = +0.3$ V. Data were fitted by equivalent circuits containing constant phase element (CPE) (Figure S4). Derived R_{ct} values are significantly lower for CMP 500, 1000, and 2000 electrodes than for the AG 500 electrode, in agreement with our previous study [17] and supported the herein reported results from CV measurements, showing the superiority of CMP BDD surfaces in comparison with non-treated AG BDD surfaces. For laser-treated electrodes, this was valid when the sp^2 carbon area fraction was less than 25%. With further increase in sp^2 carbon area fraction, R_{ct} values, on average slightly decreased for AG 500 (R_{ct} values range from 19.5 kΩ to 32.7 kΩ for electrodes with 25 to 100% sp^2 carbon) but substantially increased for CMP electrodes (from 1–4 kΩ for CMP 500–2000 electrodes with 0%–10% sp^2 carbon, and to 10–19 kΩ for CMP BDD electrodes with 100% sp^2 carbon). This indicated a slightly easier redox process on AG BDD electrodes, but a hindrance on CMP BDD electrodes (which possessed low R_{ct} values prior to laser treatment), with increasing sp^2 carbon fraction area. For both CMP and AG BDD electrodes, relatively uniform R_{ct} values were obtained after 100% surface conversion confirming the same character of the material with sp^2 carbon governing the electrochemical behaviour.

Y_0 values of all electrodes (Table 3) respect the number of charge transfer carriers and thus are increasing with increasing boron content when comparing CMP 500 to 2000 electrodes for the same sp^2 carbon area fraction (a trend recognized previously for AG BDD electrodes [3, 6,56]), and when comparing AG or CMP BDD electrodes with constant boron content with increasing sp^2 carbon area fraction. For the latter case, the increase of Y_0 is again more pronounced when the sp^2 carbon area fraction is greater than 25%. This indicates clearly that the laser-irradiated spots with sp^2 carbon contribute to the conductivity of the material, similar to other BDD electrodes containing more uniformly distributed sp^2 carbon-rich sites [57,64].

4. Conclusion

We have developed and demonstrated the universal process of sp^3 to sp^2 carbon conversion in thin diamond layers (≈ 500 nm) utilizing boron atom incorporation and IR laser material processing. This approach enables the fabrication of diamond layers with desired sp^2/sp^3 carbon ratios and their controlled lateral distribution. Advantageously, the incorporation of boron atoms leads to an increase in optical absorption in the infrared part of electromagnetic spectra and therefore reduces laser beam energy (or laser fluence) required for sp^3 to sp^2 carbon conversion, which leads to a reduction in stress of the BDD material and substrates used during laser processing. It has been shown that sp^3 to sp^2 carbon conversion is possible at relatively low laser fluences ($F_{th} \approx 1$ J cm^{-2}) and in single pulse mode. This allows tailoring of not only the surface sp^2/sp^3 ratio but also the shaping of modified spots on the surface (using Gaussian and doughnut-shaped beam profiles) with a relatively high resolution in the order of tens of micrometers due to the deterministic nature of ultrafast laser excitation of bandgap materials. In this way, advanced structuring including ring structures with central part represented by sp^3 carbon surrounded by laser-formed sp^2 carbon or networks of sp^2 carbon could be fabricated. Modified features on diamond surfaces were analysed using Raman spectroscopy, enabling the identification of optimal parameters for desired sp^3 to sp^2 carbon conversion. Additionally, this approach can be applied to other laser sources operating outside the IR region.

The electrochemical activity of laser-treated electrodes was verified for both AG (deposited at B/C ratio 500 ppm) and CMP (B/C = 500, 1000 and 2000 ppm) BDD electrodes with sp^2 carbon area fraction 0%–100%. For CMP electrodes, which possess uniform conductivity and fast HET kinetic even for surface sensitive redox marker [Fe(CN)$_6$]$^{3-/4-}$ [17], electrochemical properties are not influenced by laser irradiation when sp^3 to sp^2 carbon conversion < 25% of the electrode area. This confirms the dominant role of boron as a charge carrier at low sp^2 carbon area fractions and relatively low electrochemical activity of the laser-formed sp^2 carbon. Above this value, sp^2 carbon spots start to play a dominant role in charge transfer decelerating HET kinetics. This trend was not unambiguously seen for BDD electrode AG 500 ppm from CV measurements, which exhibit relatively uniform behaviour with varying sp^2 carbon content. From EIS measurements of CMP BDD electrodes the charge transfer resistance R_{ct} increased with increasing sp^2 carbon area fraction, which reveals that sp^2 carbon spots disrupt the reported electrochemical properties improvements gained by CM polishing. Further, significant increase in capacitance of the double layer described by Y_0 parameter was observed for both CMP and AG electrodes confirming that sp^2 carbon formed by laser irradiation served as a charge transfer carrier. Finally, the "undoped" electrode AG 0 (with minimal boron content), also showed significant electrochemical activity for sp^2 carbon area fractions > 25%.

The gained knowledge will path the way to prospective applications including construction of biosensors benefiting from attachment of the bioreceptor on the sp^2 carbon phase and detection of the electroactive product formed on this recognition component in the presence of the analyte on the sp^3 carbon phase benefiting from it is fast HET kinetics (especially for CMP BDD) and fouling resistance. In wider perspective hybrid sp^2/sp^3 carbon devices with patterned sp^2 carbon pathways could be also tested in neuroscience for controlled neuron culturing on this carbon phase. This might be useful for fabrication of devices for real-time monitoring of neurochemical and electric activity of neurons or fabrication of neural interfaces for bidirectional signal transduction for prostheses.

CRediT authorship contribution statement

J. Hrabovsky: Visualization, Investigation, Writing – original draft, Conceptualization. **M. Zelensky:** Visualization, Investigation, Writing –

original draft, Conceptualization. **J. Sladek:** Investigation, Formal analysis, Review, Writing – review & editing. **M. Zukerstein:** Investigation, Formal analysis, Review, Writing – review & editing. **J. Fischer:** Visualization, Formal analysis, Review. **K. Schwarzova-Peckova:** Writing – review & editing, Supervision, Funding acquisition, Conceptualization. **A. Taylor:** Investigation, Writing – review & editing, Funding acquisition, Conceptualization. **M. Veis:** Formal analysis, Review. **S. Mandal:** Formal analysis, Review. **O.A. Williams:** Formal analysis, Review. **N.M. Bulgakova:** Writing – review & editing, Supervision, Funding acquisition, Conceptualization.

Declaration of competing interest

The authors declare that they have no known competing financial interests or personal relationships that could have appeared to influence the work reported in this paper.

Data availability

Data will be made available on request.

Appendix A. Supplementary data

Supplementary material related to this article can be found online at https://doi.org/10.1016/j.apsusc.2023.158268.

References

[1] N. Yang, S. Yu, J.V. Macpherson, Y. Einaga, H. Zhao, G. Zhao, G.M. Swain, X. Jiang, Conductive diamond: synthesis, properties, and electrochemical applications, Chem. Soc. Rev. 48 (2019) 157–204, http://dx.doi.org/10.1039/C7CS00757D.

[2] S. Yu, S. Liu, X. Jiang, N. Yang, Recent advances on electrochemistry of diamond related materials, Carbon 200 (2022) 517–542, http://dx.doi.org/10.1016/j.carbon.2022.09.044.

[3] S. Baluchová, A. Daňhel, H. Dejmková, V. Ostatná, M. Fojta, K. Schwarzová-Pecková, Recent progress in the applications of boron doped diamond electrodes in electroanalysis of organic compounds and biomolecules – A review, Anal. Chim. Acta 1077 (2019) 30–66, http://dx.doi.org/10.1016/j.aca.2019.05.041.

[4] L.J. Simcox, R.P.A. Pereira, E.M.H. Wellington, J.V. Macpherson, Boron doped diamond as a low biofouling material in aquatic environments: Assessment of pseudomonas aeruginosa biofilm formation, ACS Appl. Mater. Interfaces 11 (2019) 25024–25033, http://dx.doi.org/10.1021/acsami.9b07245.

[5] Z. Deng, R. Zhu, L. Ma, K. Zhou, Z. Yu, Q. Wei, Diamond for antifouling applications: A review, Carbon 196 (2022) 923–939, http://dx.doi.org/10.1016/j.carbon.2022.05.015.

[6] M. Brycht, S. Baluchová, A. Taylor, V. Mortet, S. Sedláková, L. Klimša, J. Kopeček, K. Schwarzová-Pecková, Comparison of electrochemical performance of various boron-doped diamond electrodes: Dopamine sensing in biomimicking media used for cell cultivation, Bioelectrochemistry 137 (2021) 107646, http://dx.doi.org/10.1016/j.bioelechem.2020.107646.

[7] K. Zhang, H. Wang, Y. Zhao, Y. Xi, B. Liu, J. Xi, G. Shao, B. Fan, H. Lu, H. Xu, R. Zhang, N. Yan, Z. Wang, Preparation and electrochemical properties of boron-doped polycrystalline diamond film with five-fold twin structure, App. Surf. Sci. 568 (2021) 150977, http://dx.doi.org/10.1016/j.apsusc.2021.150977.

[8] K. Schwarzová-Pecková, J. Vosáhlová, J. Barek, I. Šloufová, E. Pavlova, V. Petrák, J. Zavázalová, Influence of boron content on the morphological, spectral, and electroanalytical characteristics of anodically oxidized boron-doped diamond electrodes, Electrochim. Acta 243 (2017) 170–182, http://dx.doi.org/10.1016/j.electacta.2017.05.006.

[9] S. Garcia-Segura, E. Vieira dos Santos, C.A. Martínez-Huitle, Role of sp^3/sp^2 ratio on the electrocatalytic properties of boron-doped diamond electrodes: A mini review, Electrochem. Commun. 59 (2015) 52–55, http://dx.doi.org/10.1016/j.elecom.2015.07.002.

[10] B.C. Lourencao, R.F. Brocenschi, R.A. Medeiros, O. Fatibello-Filho, R.C. Rocha-Filho, Analytical applications of electrochemically pretreated boron-doped diamond electrodes, ChemElectroChem 7 (2020) 1291–1311, http://dx.doi.org/10.1002/celc.202000050.

[11] R.L. McCreery, Advanced carbon electrode materials for molecular electrochemistry, Chem. Rev. 108 (2008) 2646–2687, http://dx.doi.org/10.1021/cr068076m.

[12] L.A. Hutton, J.G. Iacobini, E. Bitziou, R.B. Channon, M.E. Newton, J.V. Macpherson, Examination of the factors affecting the electrochemical performance of oxygen-terminated polycrystalline boron-doped diamond electrodes, Anal. Chem. 85 (2013) 7230–7240, http://dx.doi.org/10.1021/ac401042t.

[13] J. Klouda, K. Nesměrák, P. Kočovský, J. Barek, K. Schwarzová-Pecková, A novel voltammetric approach to the detection of primary bile acids in serum samples, Bioelectrochemistry 134 (2020) 107539, http://dx.doi.org/10.1016/j.bioelechem.2020.107539.

[14] J. Zavazalova, K. Prochazkova, K. Schwarzova-Peckova, Boron-doped diamond electrodes for voltammetric determination of benzophenone-3, Anal. Lett. 49 (2016) 80–91, http://dx.doi.org/10.1080/00032719.2014.1003425.

[15] E.L. Thomas, G.W. Nelson, S. Mandal, J.S. Foord, O.A. Williams, Chemical mechanical polishing of thin film diamond, Carbon 68 (2014) 473–479, http://dx.doi.org/10.1016/j.carbon.2013.11.023.

[16] E.L. Thomas, S. Mandal, E.B. Brousseau, O.A. Williams, Silica based polishing of {100} and {111} single crystal diamond, Sci. Technol. Adv. Mater. 15 (2014) 035013, http://dx.doi.org/10.1088/1468-6996/15/3/035013.

[17] M. Zelenský, J. Fischer, S. Baluchová, L. Klimša, J. Kopeček, M. Vondráček, L. Fekete, J. Eidenschink, F.-M. Matysik, S. Mandal, O. Williams, M. Hromadová, V. Mortet, K. Schwarzová-Pecková, A. Taylor, Chem-mechanical polishing influenced morphology, spectral and electrochemical characteristics of boron doped diamond, Carbon 203 (2023) 363–376, http://dx.doi.org/10.1016/j.carbon.2022.11.069.

[18] A. Taylor, P. Ashcheulov, P. Hubík, Z. Weiss, L. Klimša, J. Kopeček, J. Hrabovský, M. Veis, J. Lorinčík, I. Elantyev, V. Mortet, Comparative determination of atomic boron and carrier concentration in highly boron doped nano-crystalline diamond, Diam. Relat. Mater. 135 (2023) 109837, http://dx.doi.org/10.1016/j.diamond.2023.109837.

[19] A.W.S. Williams, E.C. Lightowlers, A.T. Collins, Impurity conduction in synthetic semiconducting diamond, J. Phys. C 3 (1970) 1727, http://dx.doi.org/10.1088/0022-3719/3/8/011.

[20] Z. Zhai, N. Huang, X. Jiang, Progress in electrochemistry of hybrid diamond/sp^2-C nanostructures, Curr. Opin. Electrochem. 32 (2022) 100884, http://dx.doi.org/10.1016/j.coelec.2021.100884.

[21] I. Vlasov, O.I. Lebedev, V.G. Ralchenko, E. Goovaerts, G. Bertoni, G. Van Tendeloo, V.I. Konov, Hybrid diamond-graphite nanowires produced by microwave plasma chemical vapor deposition, Adv. Mater. 19 (2007) 4058–4062, http://dx.doi.org/10.1002/adma.200700442.

[22] J. Davis, J.C. Baygents, J. Farrell, Understanding persulfate production at boron doped diamond film anodes, Electrochim. Acta 150 (2014) 68–74, http://dx.doi.org/10.1016/j.electacta.2014.10.104.

[23] O. Azizi, D. Hubler, G. Schrader, J. Farrell, B.P. Chaplin, Mechanism of perchlorate formation on boron-doped diamond film anodes, Environ. Sci. Technol. 45 (2011) 10582–10590, http://dx.doi.org/10.1021/es202534w.

[24] Y. Einaga, Boron-doped diamond electrodes: Fundamentals for electrochemical applications, Acc. Chem. Res. 55 (2022) 3605–3615, http://dx.doi.org/10.1021/acs.accounts.2c00597.

[25] Z.J. Ayres, A.J. Borrill, J.C. Newland, M.E. Newton, J.V. Macpherson, Controlled sp^2 functionalization of boron doped diamond as a route for the fabrication of robust and nernstian pH electrodes, Anal. Chem. 88 (2016) 974–980, http://dx.doi.org/10.1021/acs.analchem.5b03732.

[26] T.L. Read, S.J. Cobb, J.V. Macpherson, An sp^2 patterned boron doped diamond electrode for the simultaneous detection of dissolved oxygen and pH, ACS Sens. 4 (2019) 756–763, http://dx.doi.org/10.1021/acssensors.9b00137.

[27] S.J. Cobb, Z.J. Ayres, M.E. Newton, J.V. Macpherson, Deconvoluting surface-bound quinone proton coupled electron transfer in unbuffered solutions: Toward a universal voltammetric pH electrode, J. Am. Chem. Soc. 141 (2019) 1035–1044, http://dx.doi.org/10.1021/jacs.8b11518.

[28] S.J. Cobb, F.H. Laidlaw, G. West, G. Wood, M.E. Newton, R. Beanland, J.V. Macpherson, Assessment of acid and thermal oxidation treatments for removing sp^2 bonded carbon from the surface of boron doped diamond, Carbon 167 (2020) 1–10, http://dx.doi.org/10.1016/j.carbon.2020.04.095.

[29] F. Picollo, A. Battiato, E. Bernardi, A. Marcantoni, A. Pasquarelli, E. Carbone, P. Olivero, V. Carabelli, Microelectrode arrays of diamond-insulated graphitic channels for real-time detection of exocytotic events from cultured chromaffin cells and slices of adrenal glands, Anal. Chem. 88 (2016) 7493–7499, http://dx.doi.org/10.1021/acs.analchem.5b04449.

[30] K. Siuzdak, M. Ficek, M. Sobaszek, J. Ryl, M. Gnyba, P. Niedziałkowski, N. Malinowska, J. Karczewski, R. Bogdanowicz, Boron-enhanced growth of micron-scale carbon-based nanowalls: A route toward high rates of electrochemical biosensing, ACS Appl. Mater. Interfaces 9 (2017) 12982–12992, http://dx.doi.org/10.1021/acsami.6b16860.

[31] P. Wang, X. Yuan, Z. Cui, C. Xu, Z. Sun, J. Li, J. Liu, Y. Tian, H. Li, A nanometer-sized graphite/boron-doped diamond electrochemical sensor for sensitive detection of acetaminophen, ACS Omega 6 (2021) 6326–6334, http://dx.doi.org/10.1021/acsomega.0c06141.

[32] A.F. Sartori, S. Orlando, A. Bellucci, D.M. Trucchi, S. Abrahami, T. Boehme, T. Hantschel, W. Vandervorst, J.G. Buijnsters, Laser-induced periodic surface structures (LIPSS) on heavily boron-doped diamond for electrode applications, ACS Appl. Mater. Interfaces 10 (2018) 43236–43251, http://dx.doi.org/10.1021/acsami.8b15951.

[33] T. Watanabe, Y. Honda, K. Kanda, Y. Einaga, Tailored design of boron-doped diamond electrodes for various electrochemical applications with boron-doping level and sp^2-bonded carbon impurities, Phys. Status Solidi A 211 (2014) 2709–2717, http://dx.doi.org/10.1002/pssa.201431455.

[34] F. Silva, A. Gicquel, A. Tardieu, P. Cledat, T. Chauveau, Control of an MPACVD reactor for polycrystalline textured diamond films synthesis: role of microwave power density, Diam. Relat. Mater. 5 (1996) 338–344, http://dx.doi.org/10.1016/0925-9635(95)00428-9.

[35] J.M. Liu, Simple technique for measurements of pulsed Gaussian-beam spot sizes, Opt. Lett. 7 (1982) 196–198, http://dx.doi.org/10.1364/OL.7.000196.

[36] J. Hrabovsky, C. Liberatore, I. Mirza, J. Sladek, J. Beranek, A.V. Bulgakov, N.M. Bulgakova, Surface structuring of kapton polyimide with femtosecond and picosecond IR laser pulses, Interfacial Phenom. Heat Transfer 7 (2019) 113–121, http://dx.doi.org/10.1615/InterfacPhenomHeatTransfer.2019031067.

[37] M. Zukerstein, J. Hrabovsky, J. Sladek, I. Mirza, Y. Levy, N.M. Bulgakova, Formation of tubular structures and microneedles on silicon surface by doughnut-shaped ultrashort laser pulses, Appl. Surf. Sci. 592 (2022) 153228, http://dx.doi.org/10.1016/j.apsusc.2022.153228.

[38] R.S. Nicholson, Theory and application of cyclic voltammetry for measurement of electrode reaction kinetics, Anal. Chem. 37 (1965) 1351–1355, http://dx.doi.org/10.1021/ac60230a016.

[39] A.J. Bard, L.R. Faulkner, H.S. White, Electrochemical Methods: Fundamentals and Applications, third ed., Wiley, 2022.

[40] Y. Wang, J. Lin, R. Zong, J. He, Y. Zhu, Enhanced photoelectric catalytic degradation of methylene blue via TiO2 nanotube arrays hybridized with graphite-like carbon, J. Mol. Catal. A: Chem. 349 (2011) 13–19, http://dx.doi.org/10.1016/j.molcata.2011.08.020.

[41] A.T. Collins, Handbook of Industrial Diamonds and Diamond Films, Marcel Dekker, New York, 1998.

[42] T. Tomiki, F. Fukudome, M. Kaminao, M. Fujisawa, Y. Tanahara, T. Futemma, Optical spectra of $Y_3Al_5O_{12}$ (YAG) single crystals in the Vacuum Ultraviolet Region, J. Phys. Soc. Japan 58 (1989) 1801–1810, http://dx.doi.org/10.1143/JPSJ.58.1801.

[43] J. Hrabovsky, M. Kucera, L. Palousova, L. Bi, M. Veis, Optical characterization of $Y_3Al_5O_{12}$ and $Lu_3Al_5O_{12}$ single crystals, Opt. Mater. Express 11 (2021) 1218–1223, http://dx.doi.org/10.1364/OME.417670.

[44] M. Letz, A. Gottwald, M. Richter, V. Liberman, L. Parthier, Temperature-dependent Urbach tail measurements of lutetium aluminum garnet single crystals, Phys. Rev. B 81 (2010) 155109, http://dx.doi.org/10.1103/PhysRevB.81.155109.

[45] A. Taylor, L. Fekete, P. Hubík, A. Jäger, P. Janíček, V. Mortet, J. Mistrík, J. Vacík, Large area deposition of boron doped nano-crystalline diamond films at low temperatures using microwave plasma enhanced chemical vapour deposition with linear antenna delivery, Diam. Relat. Mater. 47 (2014) 27–34, http://dx.doi.org/10.1016/j.diamond.2014.05.002.

[46] J. Bonse, S. Baudach, J. Krüger, W. Kautek, M. Lenzner, Femtosecond laser ablation of silicon–modification thresholds and morphology, Appl. Phys. A 74 (2002) 19–25, http://dx.doi.org/10.1007/s003390100893.

[47] J. Sladek, I. Mirza, Laser induced damage threshold of silicon with native and artificial SiO_2 layer, Mod. Mach. Sci. J. (2019) 3579–3584, http://dx.doi.org/10.17973/MMSJ.2019_12_2019103.

[48] C. Liberatore, J. Hrabovsky, I. Miza, A.V. Bulgakov, N.M. Bulgakova, Antenna-like effect induced by surface defects upon ultrashort laser nanostructuring of silicon, Mod. Mach. Sci. J. (2019) 3594–3597, http://dx.doi.org/10.17973/MMSJ.2019_12_2019105.

[49] J. Ryl, L. Burczyk, R. Bogdanowicz, M. Sobaszek, K. Darowicki, Study on surface termination of boron-doped diamond electrodes under anodic polarization in H_2SO_4 by means of dynamic impedance technique, Carbon 96 (2016) 1093–1105, http://dx.doi.org/10.1016/j.carbon.2015.10.064.

[50] J. Foord, J.P. Hu, Electrochemical oxidation and reduction processes at diamond electrodes of varying phase purity, Phys. Status Solidi A 203 (2006) 3121–3127, http://dx.doi.org/10.1002/pssa.200671117.

[51] T. Watanabe, S. Yoshioka, T. Yamamoto, H. Sepehri-Amin, T. Ohkubo, S. Matsumura, Y. Einaga, The local structure in heavily boron-doped diamond and the effect this has on its electrochemical properties, Carbon 137 (2018) 333–342, http://dx.doi.org/10.1016/j.carbon.2018.05.026.

[52] J. Xu, Y. Yokota, R.A. Wong, Y. Kim, Y. Einaga, Unusual electrochemical properties of low-doped boron-doped diamond electrodes containing sp^2 carbon, J. Am. Chem. Soc. 142 (2020) 2310–2316, http://dx.doi.org/10.1021/jacs.9b11183.

[53] X. Yang, W. Li, S. Wang, H. Shi, X. Wang, M. Li, L. Ding, X. Zhong, J. Wang, Hybrid sp^3/sp^2 two-dimensional nanodiamonds for electrochemical ozone production, ACS EST Eng. 3 (2023) 894–905, http://dx.doi.org/10.1021/acsestengg.2c00449.

[54] R. Rozita, N. Shannon S., V. Danny E.P., L. Fernando, P. Paulius, A. Daniel, H. Ken, Impact of methane concentration on surface morphology and boron incorporation of heavily boron-doped single crystal diamond layers, Carbon 172 (2021) 463–473, http://dx.doi.org/10.1016/j.carbon.2020.10.061.

[55] K. Cinková, C. Batchelor-McAuley, M. Marton, M. Vojs, Ľ. Švorc, R.G. Compton, The activity of non-metallic boron-doped diamond electrodes with sub-micron scale heterogeneity and the role of the morphology of sp^2 impurities, Carbon 110 (2016) 148–154, http://dx.doi.org/10.1016/j.carbon.2016.09.015.

[56] T. Watanabe, T.K. Shimizu, Y. Tateyama, Y. Kim, M. Kawai, Y. Einaga, Giant electric double-layer capacitance of heavily boron-doped diamond electrode, Diam. Relat. Mater. 19 (2010) 772–777, http://dx.doi.org/10.1016/j.diamond.2010.02.022.

[57] S. Baluchová, A. Taylor, V. Mortet, S. Sedláková, L. Klimša, J. Kopeček, O. Hák, K. Schwarzová-Pecková, Porous boron doped diamond for dopamine sensing: Effect of boron doping level on morphology and electrochemical performance, Electrochim. Acta 327 (2019) 135025, http://dx.doi.org/10.1016/j.electacta.2019.135025.

[58] S. Dong, T. Kuwana, Activation of glassy carbon electrodes by dispersed metal oxide particles: I . Ascorbic acid oxidation, J. Electrochem. Soc. 131 (1984) 813, http://dx.doi.org/10.1149/1.2115705.

[59] D.S. Shishmarev, N.V. Rees, R.G. Compton, Enhanced performance of edge-plane pyrolytic graphite (EPPG) electrodes over glassy carbon (GC) electrodes in the presence of surfactants: Application to the stripping voltammetry of copper, Electroanalysis 22 (2010) 31–34, http://dx.doi.org/10.1002/elan.200900415.

[60] K.R. Kneten, R.L. McCreery, Effects of redox system structure on electron-transfer kinetics at ordered graphite and glassy carbon electrodes, Anal. Chem. 64 (1992) 2518–2524, http://dx.doi.org/10.1021/ac00045a011.

[61] I. Svancara, K. Kalcher, A. Walcarius, K. Vytras, Electroanalysis with Carbon Paste Electrodes, first ed., CRC Press, 2012.

[62] R.J. Rice, N.M. Pontikos, R.L. McCreery, Quantitative correlations of heterogeneous electron-transfer kinetics with surface properties of glassy carbon electrodes, J. Am. Chem. Soc. 112 (1990) 4617–4622, http://dx.doi.org/10.1021/ja00168a001.

[63] M.R. Deakin, K.J. Stutts, R.M. Wightman, The effect of pH on some outer-sphere electrode reactions at carbon electrodes, J. Electroanal. Chem. Interfacial Electrochem. 182 (1985) 113–122, http://dx.doi.org/10.1016/0368-1874(85)85444-7.

[64] G.P. Keeley, M.E.G. Lyons, The effects of thin layer diffusion at glassy carbon electrodes modified with porous films of single-walled carbon nanotubes, Int. J. Electrochem. Sci. 4 (2009) 794–809, URL http://www.electrochemsci.org/papers/vol4/4060794.pdf.